Computer Modeling in Engineering & Sciences

Tech Science Press

https://doi.org/10.32604/cmes.2026.087958

ARTICLE

Wind-Induced Safety Prediction Method for Truck Running on a Cross-Sea Bridge Considering Crosswind Stability

Zhiqun Yuan[1,2,3], Maoxing Zhu[2], Shihao Tan[2], Hongzheng He[2], Yongchen Peng[4], Dandan Xia[1], Huaifeng Wang[1] and Li Lin[1,*]

[1]Fujian Provincial Key Laboratory of Wind Disaster and Wind Engineering, Xiamen University of Technology, Xiamen, China
[2]School of Mechanical and Automotive Engineering, Xiamen University of Technology, Xiamen, China
[3]Fujian Provincial Key Laboratory of Advanced Design and Manufacture for Bus Coach, Xiamen University of Technology, Xiamen, China
[4]Fujian Construction Engineering Group Co., Ltd., Fuzhou, China

*Corresponding Author: Li Lin. Email: 2011110904@xmut.edu.cn

Received: 25 June 2026; Accepted: 11 September 2026; Published: 21 October 2026

ABSTRACT: Box trucks are among the most common vehicle types on cross-sea bridges and exhibit the poorest crosswind stability. Identifying the key influencing factors is an essential prerequisite for evaluating wind-induced driving safety of vehicles on bridges. First, a crosswind stability analysis and evaluation model for trucks on bridges was established using a coupled approach integrating vehicle aerodynamics and vehicle system dynamics. A systematic multi-factor quantitative assessment of lateral deviation and yaw motion responses of box trucks was then conducted. Second, a wind-induced driving safety prediction model for trucks on bridges considering multi-factor coupling effects was developed based on the Extreme Gradient Boosting (XGBoost) algorithm, enabling the evaluation of vehicle motion states under various driving conditions. The results indicate that loading condition has the most significant influence on wind-induced driving safety, followed by road adhesion coefficient, crosswind speed, and vehicle speed, while driver preview time has the least influence. The proposed wind-induced driving safety prediction model achieved an exact-match accuracy of 95.7% on the test set. Finally, an intelligent traffic management system framework for strong-wind regions was proposed, integrating real-time information perception, driving-risk assessment, hierarchical warning, and dynamic traffic control functions. By incorporating the model prediction results, the proposed framework provides a theoretical reference for intelligent traffic management and smart road development of cross-sea bridges.

KEYWORDS: Crosswind stability; box truck; wind-induced driving safety prediction; machine learning; traffic management

1 Introduction

"Green, intelligent, safe, and reliable" are the core elements in the development of high-speed transportation networks. Among the numerous factors determining the traffic safety of these networks, the impact of crosswinds cannot be ignored. In recent years, wind-induced driving accidents on highways have occurred frequently worldwide, predominantly involving trucks traveling on cross-sea bridges. With the increasing proportion of cross-sea bridges in high-speed transportation networks and the continuous advancement of smart roadway construction, new requirements have emerged for evaluating wind-induced driving safety on these bridges. The traditional "one-size-fits-all" traffic management mode can no longer meet the developmental needs of future transportation systems.

Copyright © 2026 The Authors. Published by Tech Science Press. This work is licensed under a Creative Commons Attribution 4.0 International License, which permits unrestricted use, distribution, and reproduction in any medium, provided the original work is properly cited.

The wind-induced driving safety capability of vehicles on cross-sea bridges is closely related to vehicle handling stability and driving conditions [1]. Among these, vehicle handling stability is determined by the overall vehicle design parameters and serves as the intrinsic factor affecting wind-induced driving safety [2–4]. However, the core challenge lies in addressing the strong nonlinear coupling relationship intertwined by vehicle dynamics (intrinsic factors) and extreme meteorological and complex driving conditions (extrinsic factors). Previous studies on wind-induced driving stability primarily relied on traditional physical mechanism-based evaluation methods (e.g., co-simulation of Computational Fluid Dynamics (CFD) and multibody dynamics) [5–8]. Although these methods can reconstruct the aerodynamic and dynamic evolution processes of vehicle lateral deviation, sideslip, and rollover with high fidelity, they exhibit distinct technical limitations: On the one hand, their extremely high computational costs restrict them to analyzing discrete, single-variable static conditions, neglecting the dynamic interactions of multi-source factors such as crosswind speed, vehicle speed, payload, road adhesion coefficient, and driver preview. On the other hand, the massive computational demand prevents these traditional physical models from being deployed online, making it difficult to satisfy the urgent requirements of intelligent transportation systems (ITS) for real-time dynamic prediction.

In recent years, to overcome the computational bottlenecks of physical simulations, machine learning (ML)-based traffic risk prediction models have been widely introduced [9,10]. Compared with traditional methods, these data-driven models (e.g., Random Forests) have demonstrated remarkable multivariate nonlinear mapping capabilities and millisecond-level real-time inference speeds. However, most existing ML traffic risk evaluation models act as "black-box" models lacking physical constraints. Furthermore, their training data predominantly originate from historical macroscopic accident statistics, failing to deeply integrate the physical boundaries of vehicle aerodynamics and system dynamics [11–14] at the fundamental level. Consequently, when confronted with long-tail hazardous scenarios lacking historical training samples, such as extreme crosswinds on cross-sea bridges (e.g., 32.7 m/s), purely data-driven ML models are highly susceptible to overfitting or generating overly optimistic predictions. Thus, the safety margins they output lack reliable support from physical mechanisms.

To bridge the gap between computationally expensive physical simulations and purely data-driven models, an abundance of research on fluid mechanics-machine learning hybrid methods and Physics-Informed Machine Learning (PIML) has recently emerged in the literature [15,16]. Recent studies indicate that combining fundamental fluid mechanics with neural networks can significantly accelerate the prediction of complex flow fields while maintaining strict physical consistency. Nevertheless, a critical review of the current literature reveals that the application of such hybrid methods to the specific issue of crosswind driving safety remains limited. The highly nonlinear interactions within the "wind-vehicle-bridge" system are exceedingly difficult to incorporate into standard physical loss functions. In addition, although ITS increasingly adopts advanced deep learning algorithms for macroscopic traffic flow optimization [17,18], its active safety and early warning modules often lack the micro-aerodynamic inputs and transient vehicle dynamics information required to cope with extreme weather conditions.

The methodological novelty and main contributions of this study are reflected in the following three aspects: Firstly, by discarding traditional macroscopic statistical data and utilizing the co-simulation of CFD and TruckSim, the coupling relationship among aerodynamic forces, tire cornering forces, and complex driving conditions is accurately quantified. This approach provides a high-fidelity underlying data source, supported by rigorous dynamic theory, for machine learning. Secondly, the eXtreme Gradient Boosting (XGBoost) algorithm is introduced to systematically analyze the interactive effects of multi-source heterogeneous variables—including extreme crosswind speed, vehicle speed, payload, road adhesion capability, and driver response characteristics—thereby breaking the limitations of the "independent single-factor analysis" prevalent in traditional studies. Finally, the proposed model effectively overcomes the technical bottleneck

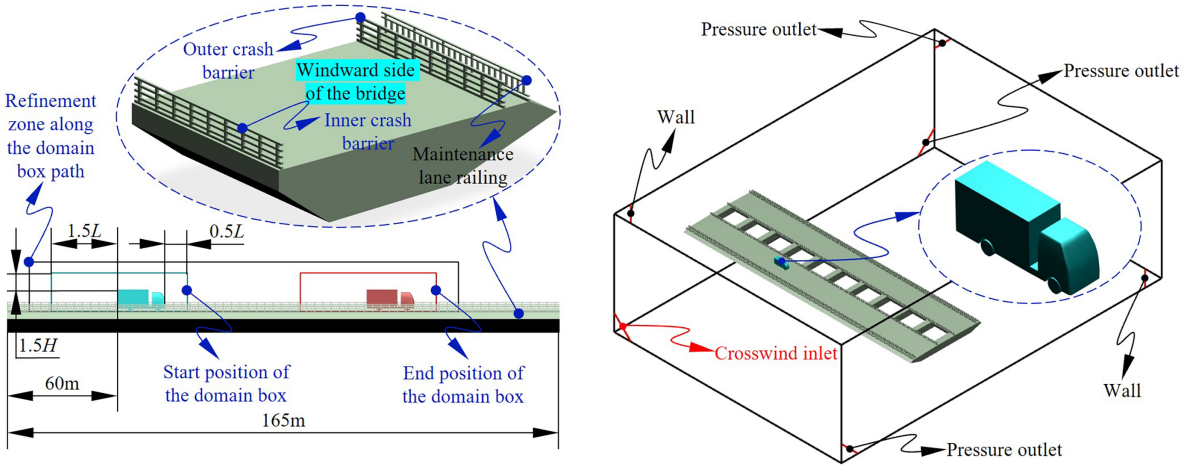
wherein traditional dynamic simulations fail to achieve online computation. More importantly, through an in-depth analysis of feature importance and classification decision boundaries, this study verifies that the data-driven prediction results maintain high physical consistency with underlying vehicle dynamic thresholds (e.g., the critical instability points of lateral displacement and yaw angle). This provides a reliable methodological foundation for implementing refined and active dynamic traffic management on cross-sea bridges in the future.

In summary, a distinct gap exists in the current evaluation system between the "rigor of physical mechanisms" and the "efficiency of multi-factor real-time prediction". To resolve this challenge and fill the relevant research gaps, drawing upon the international cutting-edge theory of "Physics-Informed Machine Learning (PIML)" [19–23], this study adopts a research approach that integrates physical simulation with data-driven methods. Focusing on box trucks, a novel wind-induced driving safety prediction framework for cross-sea bridges is proposed.

2 Computational Model

2.1 Geometric Model

With reference to the *T/CSAE 112-2019 Technical Specification for Passenger Car Aerodynamic Simulation*, a geometric model of a box truck driving on a bridge under crosswind conditions was established using UG software, as depicted in Fig. 1a. The length (L), width (W), and height (H) of the box truck are 8.5, 2.4, and 3.9 m, respectively. The vehicle was positioned in the middle lane of the bridge. The bridge is a hybrid girder cable-stayed bridge with a gap of 12.8 m between the left and right decks, and the driving lane width is 3.75 m. The auxiliary structures on the bridge deck include maintenance walkway guardrails (1.2 m in height) and crash barriers (1.5 m in height), both of which have a wind permeability (porosity) of 75%. This permeability reflects the actual solid blockage effect of the bridge railings, indicating that the solid components account for approximately 25% of the total projected windward area. The length of the bridge segment is 165 m, and its clearance above sea level is 35 m. The inlet of the computational domain is located 50 m from the windward side of the bridge. The inlet wind direction was strictly defined as a pure crosswind, maintaining a constant 90° angle with the longitudinal driving trajectory of the vehicle. The outlet is positioned 150 m from the leeward side of the bridge, and the initial position of the truck is 60 m from the end face of the bridge's computational domain. The specific boundary condition settings are illustrated in Fig. 1b, ensuring a computational domain blockage ratio of less than 5%.



(a) Geometric Model **(b)** Computational Domain

Figure 1: Geometry models for bridge traffic.

2.2 Grid Independence Study

Prior to conducting simulations under various conditions, performing a grid independence test is essential to ensure the reliability and accuracy of the Computational Fluid Dynamics (CFD) results. This process verifies that variations in the grid resolution do not significantly affect the stability of the simulation outcomes. For the model of the box truck on the bridge, four distinct meshing schemes were evaluated. Aerodynamic drag, aerodynamic side force, and aerodynamic lift were utilized as key indicators to assess the performance of each scheme, while strictly maintaining consistent boundary conditions throughout the simulations. The four meshing schemes are detailed as follows:

- Scheme 1: A relatively large global mesh size was adopted.
- Scheme 2: Local mesh refinement was applied to the crash barriers and maintenance walkway guardrails of the bridge structure.
- Scheme 3: Building upon Scheme 2, further mesh refinement was implemented on the auxiliary structures of the half-bridge where the box truck is located.
- Scheme 4: Mesh refinement was comprehensively applied to the auxiliary structures on both sides of the bridge.

As indicated by the results in Table 1, the differences in the aerodynamic forces among Schemes 2–4 are negligible and fall well within the permissible error margin. This demonstrates that the discretization error is sufficiently small, and any further mesh refinement is unlikely to yield significant improvements. Considering the comprehensive trade-off between computational accuracy and computational cost, this study selected Scheme 3 as the optimal mesh configuration for the subsequent CFD simulations. While providing the necessary spatial resolution, this scheme maximizes computational efficiency. Consequently, it prevents unnecessary consumption of computational resources while guaranteeing the reliability of the simulation results, thereby achieving an optimal balance between accuracy and efficiency.

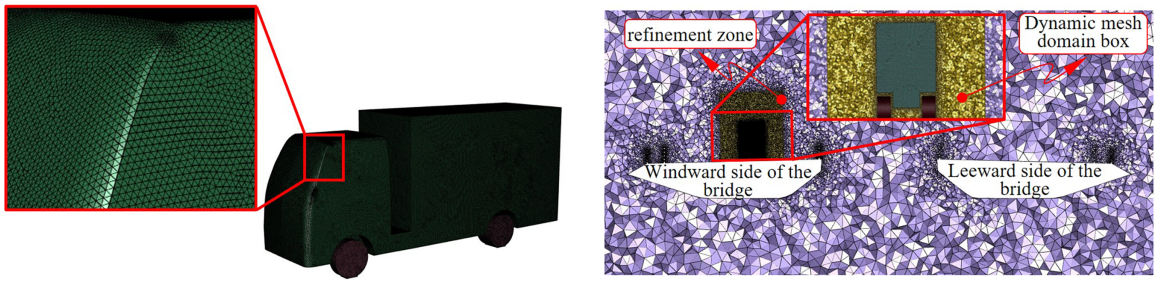
Table 1: Meshing schemes.

	Scheme 1	Scheme 2	Scheme 3	Scheme 4
Number of elements ($\times 10^4$)	3059	3301	3793	4310
Drag coefficient	0.157	0.171	0.176	0.179
Side force coefficient	2.456	2.533	2.544	2.550
Lift coefficient	0.170	0.162	0.174	0.178

2.3 Calculation Method of Aerodynamic Characteristics

The computations were performed in the commercial CFD software Fluent. To enhance computational efficiency, a dynamic mesh box was employed to simulate the motion of the truck, with dimensions of 3L in length, 3W in width, and 2.5H in height. The computational domain was discretized using triangular surface meshes and tetrahedral volume meshes in Fluent Meshing [24]. Following the grid independence verification, the total number of volume cells reached 37.93 million. To clearly illustrate the high-density mesh structure, the detailed mesh configuration and its local magnified views are presented in Fig. 2. Specifically, the external background volume mesh sizes ranged from 512 to 1024 mm, while the volume meshes along the vehicle's motion trajectory were refined to 256 mm. Furthermore, the internal moving domain box surrounding the truck was further refined to a range of 64–128 mm. The surface mesh sizes of the bridge's auxiliary structures and the vehicle body were strictly controlled within the ranges of 32–64 mm and 16–32 mm, respectively (Fig. 2b). To accurately capture the near-wall shear flow and boundary layer

separation phenomena at the sharp edges of the box truck, 6 layers of prismatic boundary layer meshes were generated on the vehicle surface. The height of the first cell layer was set to 1 mm, with a growth rate of 1.1.



(a) Face Mesh **(b)** Body Mesh

Figure 2: Mesh models for bridge traffic.

In the inlet boundary conditions, the effects of the local terrain and topography at the bridge site were neglected. Referring to relevant automotive aerodynamic standards and combining the flow field parameters of the wind tunnel tests, the turbulence intensity was set to 0.5%. This value was strictly selected to maintain consistency with the uniform and smooth flow conditions of the wind tunnel facility used for the subsequent methodological validation. Although the wind environment in natural open sea areas typically exhibits higher turbulence intensities (e.g., 10%–18%). In automotive aerodynamics, however, the primary purpose of selecting a turbulence intensity of 0.5% is to maintain consistency with the uniform and smooth inflow conditions commonly adopted in wind-tunnel tests and to establish a reproducible deterministic aerodynamic baseline. Low free-stream turbulence generally induces more severe flow separation on bluff bodies, thereby generating more hazardous mean aerodynamic side forces [25,26].

Therefore, the low-turbulence condition adopted in this study is primarily regarded as a deterministic reference baseline for evaluating the mean or quasi-steady aerodynamic response under a prescribed uniform crosswind. In actual cross-sea bridge environments, multiscale atmospheric turbulence and stochastic gusts may induce transient load peaks exceeding those predicted by the present model. The potential influence of these effects is further discussed in the limitations section of this study.

Box trucks are typical bluff bodies with sharp edges. Under a 90° strong crosswind, the flow separation point on the windward side of the vehicle body is primarily forced by the sharp geometric angles of the cargo box, rather than progressively evolving from an adverse pressure gradient within the boundary layer. Therefore, for crosswind conditions on bluff bodies where the separation point is already locked by geometric features, the accuracy advantage of the SST model in predicting curved surface boundary layer separation is not significant. In contrast, the Realizable model demonstrates superior adaptability when handling wake regions characterized by strong streamline curvature, large-scale vortices, and rotational flows. Furthermore, it exhibits extremely high numerical stability during lengthy transient physical time-step solving [27].

Therefore, the Realizable k-ε turbulence model was adopted for the numerical simulation. To ensure the rigor and reproducibility of the CFD simulation, the specific boundary conditions and strict convergence criteria were explicitly defined. At the inlet of the computational domain, a uniform velocity profile was prescribed to maintain consistency with the low-turbulence-intensity baseline condition (0.5%) described above. For the near-wall treatment coupled with the Realizable k-ε model, the standard wall function was employed. Since the box truck is a typical bluff body, strong stagnation, flow separation, and low-speed flow regions exist around the vehicle. Therefore, the y^+ values on the vehicle surface exhibit spatial variations, ranging approximately from 2 to 150. Most regions treated with the wall function are located within or close

to the logarithmic layer, while locally lower y^+ values mainly occur in stagnation regions, separation zones, and local low-speed flow regions.

In addition, strict convergence criteria were implemented in this study. The pressure–velocity coupling was solved using the SIMPLE algorithm with the second-order upwind discretization scheme. A simulation case was considered converged only when the residuals reached the order of 10^{-5}, and the monitored aerodynamic forces and moments exhibited fluctuations of less than 5% within the final 1000 iterations.

Validated by wind tunnel tests of the bridge deck wind environment, the computational accuracy meets the requirements for engineering applications. Details of the relevant governing equations can be found in the literature [5,27]. The vehicle speeds for the simulations are set from 40 to 100 km/h in increments of 20 km/h. The crosswind speeds are set to 17.2, 20.8, 24.5, 28.5, and 32.7 m/s, respectively. The time step is set to 0.001 s, and the flow field reaches a stable state after the truck travels for 1.5 s.

To accurately quantify the crosswind effects, the aerodynamic loads acting on the vehicle are defined by six components. This study establishes a unified aerodynamic coordinate system with its origin positioned at the vehicle's center of mass (o), as illustrated in Fig. 3. The mathematical relationships between the aerodynamic forces/moments and their corresponding dimensionless coefficients are formulated in Eqs. (1) and (2) as follows:

$$F_i = \frac{1}{2} C_i \rho v^2 A \tag{1}$$

$$M_i = \frac{1}{2} C_{Mi} \rho v^2 A l \tag{2}$$

where F_i and M_i denote the aerodynamic forces (aerodynamic drag F_D, aerodynamic side force F_S, aerodynamic lift F_L) and aerodynamic moments (aerodynamic rolling moment M_{RM}, aerodynamic pitching moment M_{PM}, aerodynamic yawing moment M_{YM}), respectively; C_i represents the dimensionless aerodynamic force coefficients (drag coefficient C_D, side force coefficient C_S, lift coefficient C_L), and C_{Mi} represents the dimensionless aerodynamic moment coefficients (rolling moment coefficient C_{RM}, pitching moment coefficient C_{PM}, yawing moment coefficient C_{YM}); v is the relative velocity between the vehicle and the crosswind; A is the frontal reference area of the truck; and l is the characteristic length (wheelbase).

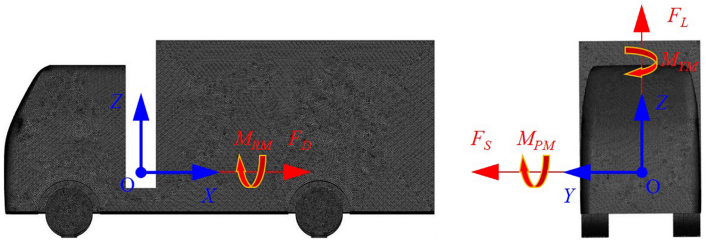


Figure 3: Aerodynamic coordinate system.

2.4 Validation of the Numerical Method

To verify the accuracy of the numerical calculation method proposed in this paper, this study compared the experimental data obtained from the wind tunnel laboratory at Xiamen University of Technology (Fig. 4). The numerical simulation adopted the same meshing scheme, boundary conditions, and solver settings as the wind tunnel experiment to establish the corresponding computational model. In the wind tunnel experiment, both the bridge box girder and the vehicle model adopted a geometric scale ratio of 1:20. The dimensions of the wind tunnel test section are 25.0 m in length, 6.0 m in width, and 3.6 m in height. To ensure the reliability of the test results, the aerodynamic blockage ratio was strictly controlled below 5%.

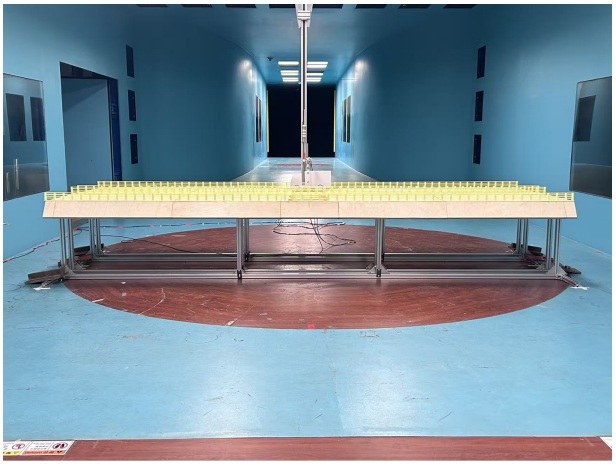


Figure 4: Wind tunnel experiment.

Regarding the fundamental physical layout, the vehicle model was rigidly mounted in a stationary state on the bridge deck. The six-component aerodynamic forces and moments acting on the truck model were measured utilizing a high-precision internal six-component aerodynamic balance. A Cobra three-dimensional probe was primarily employed to monitor the incoming crosswind speed; data acquisition commenced once the incoming flow reached the specified test conditions and stabilized. The data acquisition system recorded the turbulent force signals at a sampling frequency of 1000 Hz, with a recording duration of 60 s for each test scenario. The calibrated incoming crosswind speed during the experiment was 20.8 m/s, and the angle between the incoming flow direction and the longitudinal axis of the bridge was set to 90° to simulate extreme crosswind conditions.

Through comparative analysis, the numerical simulation results and the wind tunnel experimental results exhibit a good agreement in terms of geometric, Reynolds number, and kinematic similarities, as depicted in Fig. 5. Here, F_D denotes the aerodynamic drag, F_S represents the aerodynamic side force, M_{RM} is the aerodynamic rolling moment, and M_{YM} indicates the aerodynamic yawing moment. The data comparison demonstrates that the simulation accuracy of the crosswind computational model proposed in this study satisfies the requirements for engineering applications.

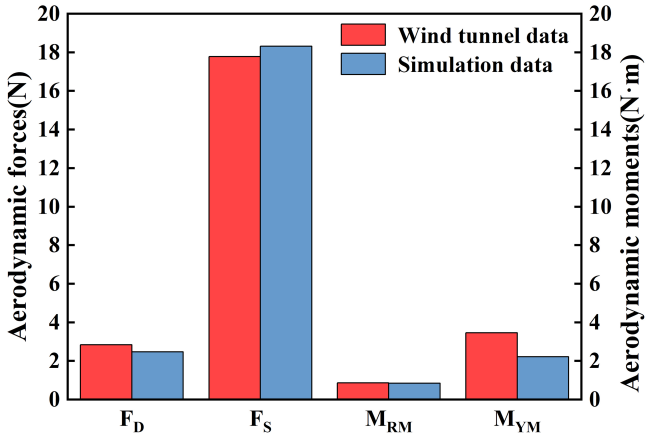


Figure 5: Comparison between numerical simulation and experimental data.

2.5 Calculation Method of Crosswind Stability

A multibody vehicle dynamics model of the box truck was established in TruckSim, and an idealized step gust was applied through the aerodynamic module. No additional linear or exponential rise/decay process was introduced during wind loading or unloading. The crosswind direction was always perpendicular to the vehicle longitudinal driving direction, corresponding to a wind angle of 90°. The gust was applied at 2 s and removed at 5 s, resulting in a duration of 3 s, and the total simulation time was set to 10 s. Although the idealized step gust does not reproduce the stochastic fluctuations and finite rise time of natural gusts, its abrupt onset and removal provide a deterministic excitation for examining the transient response of the vehicle under prescribed crosswind conditions.

In the actual implementation, the stabilized mean values of the six-component aerodynamic forces and moments obtained from CFD simulations under different operating conditions were converted into dimensionless aerodynamic coefficients (Fig. 6) and imported into TruckSim. Functional relationships were established using aerodynamic sideslip angle, crosswind speed, vehicle speed, and other relevant variables. Based on the vehicle motion parameters and the prescribed crosswind input, TruckSim calculates the corresponding aerodynamic forces and moments acting at the vehicle center of gravity. Through this conversion procedure, the aerodynamic forces and moments calculated for each operating condition in the CFD model are ensured to be consistent with those actually applied at the center of gravity in the TruckSim model. This method has been widely validated in classical "wind-vehicle-bridge" dynamic studies [28].

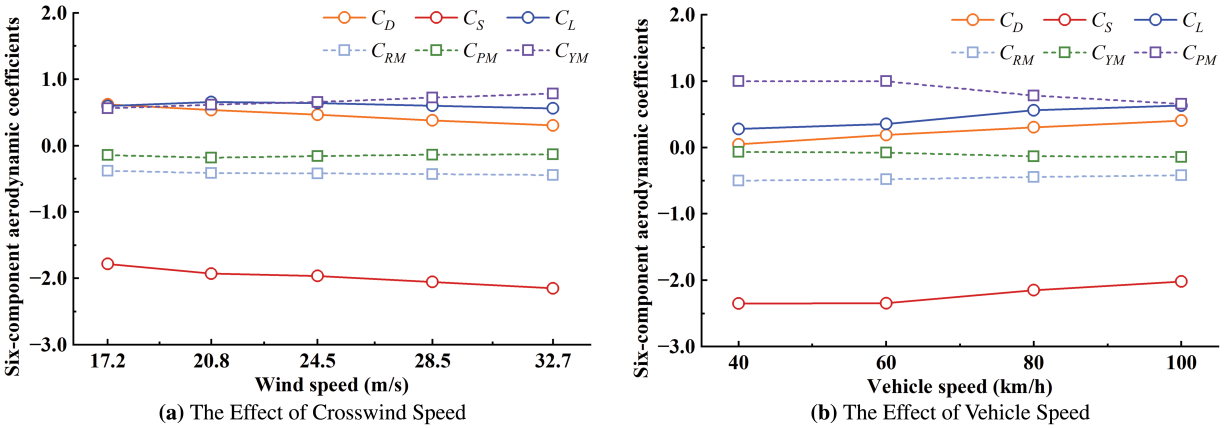


Figure 6: Aerodynamic coefficients of the box truck under different crosswind and vehicle speeds.

It should be noted that this quasi-steady approach does not iteratively update the 3D CFD mesh to reflect the vehicle's roll angle in real-time (i.e., a fully two-way fluid-structure interaction). However, existing vehicle dynamics literature indicates that prior to catastrophic rollover, the variations in the vehicle's roll and yaw angles are generally small [29]. The differences between the quasi-steady approximation and fully unsteady aerodynamic loads remain limited. Furthermore, the errors introduced by neglecting the flow field deformation caused by vehicle roll fall well within the acceptable engineering margins for vehicle stability evaluation [30].

In the closed-loop control of vehicle dynamics, the standardized driver preview control model built into the TruckSim software was directly utilized for feedback control under crosswind conditions. The underlying algorithm of this module is based on the classical MacAdam optimal preview control theory [31]. Its mathematical core involves solving an objective function that minimizes the integral of the tracking error over the future preview time horizon. By minimizing this objective function, the underlying algorithm

of TruckSim can calculate the optimal steering wheel angle in real-time, thereby accurately simulating the driver's steering wheel corrections and trajectory maintenance under sudden extreme crosswind changes. To accurately capture the dynamic response of the vehicle, the contact interaction between the truck wheels and the bridge deck is governed by the semi-empirical tire model built into TruckSim 2019, which is the software's standard default tire model. This model dynamically calculates the longitudinal and cornering forces of the tires based on the real-time vertical wheel load, tire slip angle, and specific road adhesion capability, strictly adhering to the friction ellipse boundaries. Except for the road adhesion coefficient explicitly varied in this study, all other tire parameters were kept unchanged across all simulated operating conditions. The preview times were set to 1.0, 1.4, and 2.0 s, respectively. The road adhesion coefficient ranged from 0.1 to 0.9, analyzed at intervals of 0.1. A total of 2764 sets of dynamic analysis results were obtained, and the analysis conditions are illustrated in Fig. 7. The main parameter settings of the box truck are as follows: the sprung mass is 4455 kg; the vehicle body roll inertia is 2283.9 kg·m^2; the pitch inertia is 35,402.8 kg·m^2; and the yaw inertia is 34,802.6 kg·m^2. In the unladen state, the center of gravity (CG) is located 1250 mm from the front axle and 1175 mm above the ground. In the fully laden state, the CG is located 3280 mm from the front axle and 1935 mm above the ground, with a full load mass of 9000 kg. All other models and parameters were set to the software default settings. To ensure the reproducibility of the machine learning framework, the data sampling scheme and computational strategy must be explicitly defined. A significant challenge faced in this study is the massive computational cost associated with transient 3D CFD simulations. Solving 2764 operating conditions purely through CFD is computationally prohibitive. Therefore, an aerodynamic-dynamic decoupled workflow was adopted.

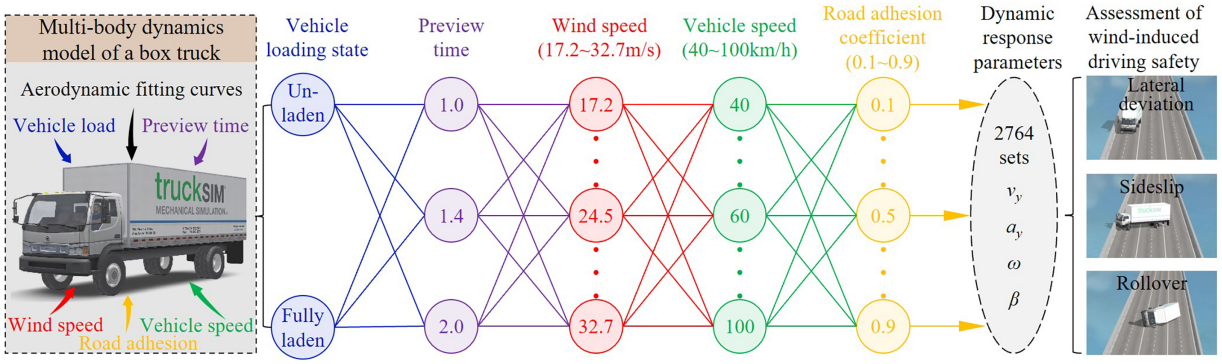


Figure 7: Parameter framework and workflow for crosswind vehicle dynamics simulations.

To enhance computational efficiency, a total of 20 transient scenarios were calculated, comprising 5 crosswind speeds and 4 vehicle speeds. The aerodynamic inputs used in the TruckSim dynamic simulations were directly derived from the CFD simulation results (Fig. 6).

The vehicle dynamics dataset in this study was constructed using a sequential Fluent–TruckSim simulation framework. First, the aerodynamic six-component force and moment coefficients of the box truck under different crosswind and vehicle-motion conditions were obtained through CFD simulations (Fig. 6), and the corresponding aerodynamic parameters were then imported into the TruckSim 2019 aerodynamics module. Based on this aerodynamic database, batch vehicle-dynamics simulations were conducted by varying five major parameters, including crosswind speed, vehicle speed, loading condition, road adhesion coefficient, and driver preview time. The parameter ranges considered in this study were as follows: crosswind speed, 17.2–32.7 m/s; vehicle speed, 40–100 km/h; loading condition, including unladen and laden states; road adhesion coefficient, 0.1–0.9; and driver preview time, 1.0, 1.4, and 2.0 s. For each operating condition,

TruckSim was used to calculate the lateral, yaw, and roll dynamic responses of the vehicle. Each simulation record was then assigned a state label according to the criteria for lateral deviation, sideslip, and rollover defined below, ultimately forming the dataset used for subsequent machine-learning analysis. During the batch generation of these automated Multi-Body Dynamics (MBD) simulations, a minority of scenarios were mathematically excluded. The excluded cases mainly corresponded to "pre-crosswind failure" scenarios. During the data-quality screening process, if the vehicle had already satisfied any of the criteria for lateral deviation, sideslip, or rollover before the prescribed crosswind was applied at (t = 2) s, the corresponding case was classified as "instability prior to crosswind application." Because such instability occurred before the onset of the external crosswind excitation and therefore could not be attributed to crosswind effects, these cases were excluded from the subsequent analysis of wind-induced driving safety. After data screening, a total of 2764 valid vehicle-dynamics records were retained for subsequent machine-learning analysis. The dataset preserved the naturally occurring class distribution of the investigated operating conditions, and no artificial oversampling or undersampling was applied to enforce class balance among the different risk categories.

3 Analysis of Aerodynamic Characteristics of Vehicle on Bridge

As shown in Figs. 8 and 9, the velocity-magnitude and pressure distributions around the box truck under different crosswind speeds and vehicle speeds are presented, respectively. Specifically, the velocity contours in Fig. 8 represent the magnitude of the three-dimensional velocity vector, rather than the velocity component along any individual coordinate direction. As evident from Fig. 8, influenced by the splitter plates and guardrails on the windward side of the bridge, a highly effective airflow shielding zone is formed within the height of the vehicle driving space, where the crosswind speed on the bridge deck is significantly lower than the incoming free-stream velocity. On the windward bridge deck, lanes situated further from the windward edge exhibit a taller airflow shielding zone, resulting in a lower equivalent crosswind speed for those lanes. The high wind speeds around the bridge are primarily concentrated at the bottom of the bridge structure. With an increase in crosswind speed, the flow velocity around the top windward edge of the box truck gradually increases. Concurrently, both the airflow stagnation region on the windward side and the airflow separation region on the leeward side expand progressively. As the vehicle speed increases, the airflow velocity around the box truck gradually rises, with the most pronounced changes occurring above the vehicle roof.

As illustrated in Fig. 9, the positive pressure regions on the box truck are predominantly concentrated on the right front section and the upper windward side, whereas the negative pressure regions are primarily distributed across the roof and the leeward side. With escalating crosswind speeds, the positive pressure zone on the windward side, as well as the negative pressure zones on the roof and leeward side, gradually expand. Conversely, as the vehicle speed increases, the positive pressure zone on the windward side gradually diminishes, while the positive pressure zone on the right side of the vehicle front enlarges. Meanwhile, both the area and magnitude of the negative pressure on the vehicle roof and leeward side progressively intensify. The variations in wind speed result in significant differences in the six-component aerodynamic forces acting on the truck, as depicted in Fig. 6.

According to Fig. 6a, the aerodynamic side force coefficient, rolling moment coefficient, and yawing moment coefficient of the truck all exhibit an upward trend with increasing crosswind speed. Conversely, the aerodynamic drag coefficient gradually decreases as the wind speed increases. Furthermore, the aerodynamic lift coefficient and pitching moment coefficient display a non-monotonic trend, initially increasing and subsequently decreasing with higher crosswind speeds. When the vehicle operates at a high speed (e.g., 80 km/h), close attention must be paid to the variations in aerodynamic forces and moments. The analysis results reveal that while the variation in wind speed has a minimal impact on the aerodynamic drag, its effects on the other aerodynamic forces and moments are remarkably significant. Specifically, when the

crosswind speed decreases from 32.7 to 17.2 m/s, the aerodynamic side force and aerodynamic lift are reduced by 58.1% and 45.9%, respectively. Correspondingly, the aerodynamic rolling moment, pitching moment, and yawing moment decrease by 56.5%, 46.8%, and 63.9%, respectively.

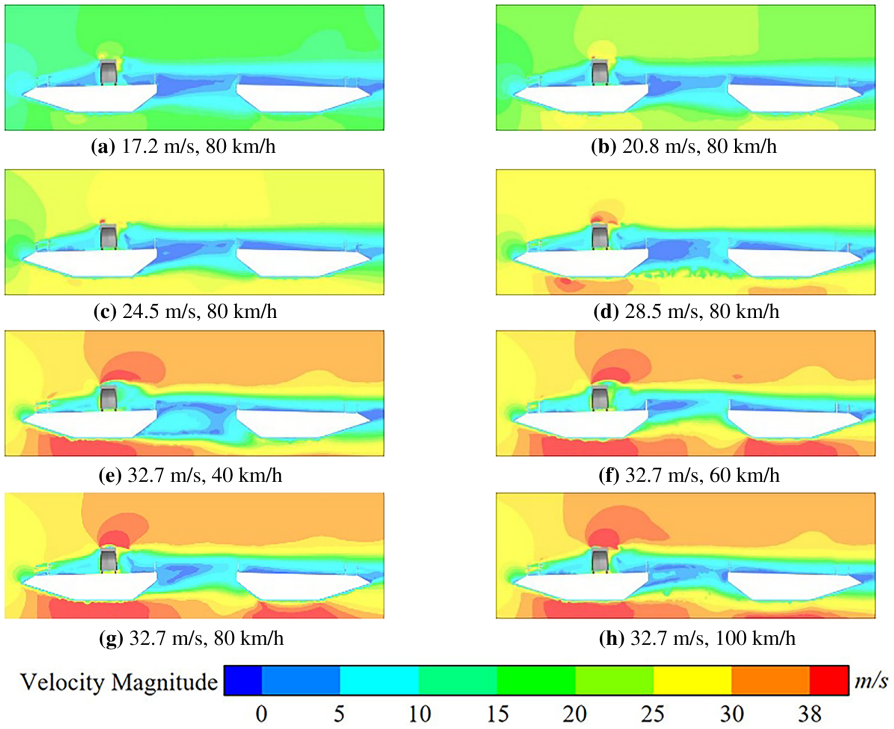


Figure 8: Velocity-magnitude contours of the truck under different crosswind and vehicle speeds.

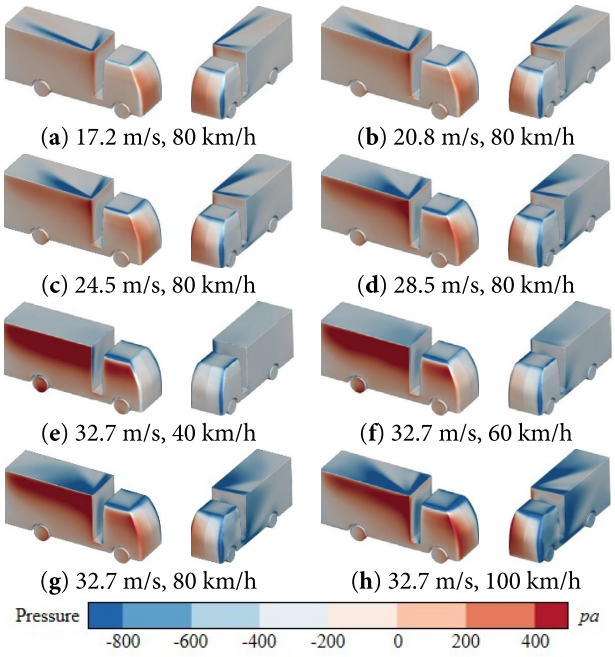


Figure 9: Surface pressure contours of the box truck under different crosswind and vehicle speeds.

As indicated by Fig. 6b, the aerodynamic drag coefficient (C_D), lift coefficient (C_L), and pitching moment coefficient (C_{PM}) of the truck all increase with the escalation of vehicle speed, whereas the aerodynamic side force coefficient, rolling moment coefficient, and yawing moment coefficient gradually decrease as the vehicle speed increases. Under a severe crosswind speed (32.7 m/s), the variation in vehicle speed exerts a minor influence on the aerodynamic yawing moment. However, the changes in the other aerodynamic forces and moments are extraordinarily significant. It is imperative to strictly distinguish between these dimensionless coefficients and the actual dimensional aerodynamic loads. When the vehicle speed is reduced from 100 to 40 km/h, although the side force and rolling moment coefficients increase, the sharp decline in dynamic pressure (which is proportional to the square of the relative velocity) dominates the overall aerodynamic interaction. Consequently, the absolute aerodynamic forces and moments decrease substantially. Specifically, the aerodynamic drag, side force, and lift are reduced by 92.1%, 24.6%, and 71.6%, respectively, while the aerodynamic rolling moment and pitching moment decrease by 23.3% and 70.3%, respectively.

The underlying cause of this phenomenon can be observed from the surface pressure contours in Fig. 9. The prominent positive pressure region on the windward side of the truck is strictly confined to the middle and upper sections of the cargo box, with no high-pressure accumulation occurring on the lower half of the vehicle body. This physical phenomenon profoundly reveals the shielding effect of the bridge deck maintenance walkway guardrails and crash barriers. They induce severe stagnation and kinetic energy dissipation in the near-deck flow field. Referring to the study by Yuan et al. [32] regarding the equivalent crosswind speed integral model, the relationship is expressed as Eq. (3).

$$V_{eff} = \sqrt{\frac{1}{z_r}\int_0^{z_r} V^2(z)dz} \tag{3}$$

When the environmental baseline crosswind speed reaches the extreme value of 24.5 m/s, the actual equivalent effective crosswind speed acting on the body of the truck traveling in the second lane decays drastically to approximately 10.3 m/s. Within the 4 m vertical space of the second windward lane, the equivalent crosswind speed is substantially reduced by 57.85% compared to the baseline incoming free-stream velocity. By the same rationale, it can be inferred that even under a simulated extreme crosswind speed of 32.7 m/s, the actual crosswind speed experienced on the bridge deck will not reach such a high magnitude.

4 Analysis of Crosswind Stability of Box Trucks

A subset of data was selected from the 2764 sets of dynamic analysis results for detailed analysis, aiming to investigate the influence patterns of crosswind speed, vehicle speed, road adhesion coefficient, vehicle payload, and driver preview time on the crosswind stability of the vehicle.

4.1 Effect of Crosswind Speed

Fig. 10 illustrates the influence patterns of crosswind speed variations on the crosswind stability of the unladen box truck, where the vehicle speed is 80 km/h, the road adhesion coefficient is 0.9, and the preview time is 1.4 s. At the moments when the gust initiates and dissipates, the lateral acceleration of the truck exhibits abrupt changes, and the yaw rate increases significantly. A higher crosswind speed results in greater aerodynamic loads, leading to more pronounced lateral deviation and yaw motions of the truck. At the instant of crosswind impact, the peak values of lateral acceleration under different crosswind speeds are 0.13, 0.17, 0.21, 0.26, and 0.33 g, respectively. The truck gradually deviates from its intended driving trajectory, with the lateral displacement of its center of mass progressively increasing. The peak lateral displacements under varying crosswind speeds reach 0.14, 0.17, 0.19, 0.23, and 0.29 m, respectively. Approximately 0.5 s after the

onset of the crosswind, the yaw rate reaches its peak. After the crosswind dissipates, influenced by the driver's feedback control, the yaw rate undergoes a reverse increase before gradually converging to a stable state under continuous driving feedback control. Affected by both the crosswind and the driving feedback, the peak yaw rates under different crosswind conditions are 1.91°/s, 2.61°/s, 4.69°/s, 6.34°/s, and 7.87°/s, respectively. Furthermore, as the crosswind speed increases, the occurrence time of these peak values is delayed.

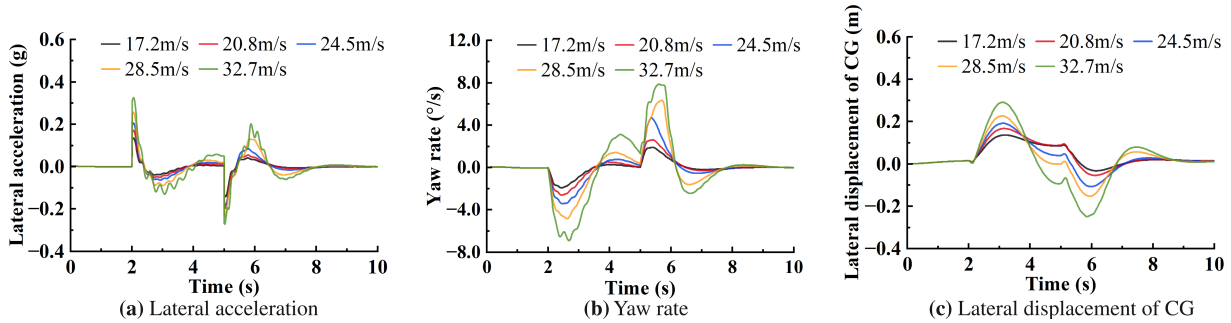


Figure 10: Effect of crosswind speed on crosswind stability of truck.

4.2 Effect of Vehicle Speed

Fig. 11 illustrates the influence patterns of vehicle speed variations on the crosswind stability of the unladen box truck, where the crosswind speed is 32.7 m/s, the road adhesion coefficient is 0.9, and the preview time is 1.4 s. A higher vehicle speed generates greater aerodynamic loads, resulting in more pronounced lateral deviation and yaw motions of the truck. At the instant of crosswind impact, the peak values of lateral acceleration under different vehicle speeds are 0.27, 0.31, 0.33, and 0.36 g, respectively, while the peak yaw rates are 4.99°/s, 7.62°/s, 7.87°/s, and 9.19°/s, respectively. The truck gradually deviates from its intended driving trajectory, with the lateral displacement of its center of mass progressively increasing. The peak lateral displacements under varying vehicle speeds reach 0.13, 0.19, 0.29, and 0.43 m, respectively. Therefore, reducing vehicle speed is highly effective in improving the crosswind stability of the truck. Furthermore, a lower vehicle speed corresponds to a shorter time required for the truck to reach a stable state after the crosswind impact.

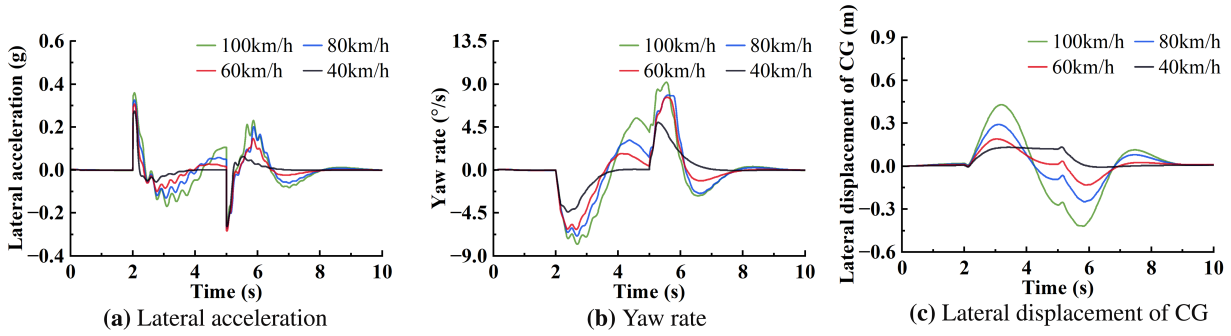
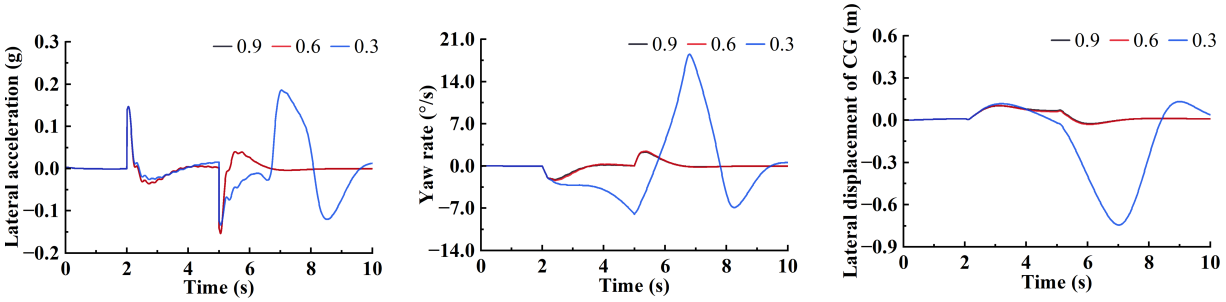


Figure 11: Effect of vehicle speed on crosswind stability of truck.

4.3 Effect of Road Adhesion

Fig. 12 illustrates the influence patterns of the road adhesion coefficient on the crosswind stability of the unladen box truck, where the crosswind speed is 20.8 m/s, the vehicle speed is 60 km/h, and the preview time is 1.4 s. When the road adhesion capability is sufficient, the impact of the adhesion coefficient on

crosswind stability is essentially negligible. At adhesion coefficients of 0.9 and 0.6, the peak values of lateral acceleration of the truck during the crosswind action are both 0.15 g, the peak yaw rates are 2.29°/s and 2.44°/s, respectively, and the peak lateral displacements are both 0.10 m. From the perspective of vehicle and tire dynamics, this phenomenon occurs because the lateral acceleration induced by the aerodynamic wind loads (approximately 0.15 g) is far below the lateral friction limits provided by μ = 0.9 and μ = 0.6. Under these operating conditions, the tires operate entirely within the linear region of their cornering stiffness curves. Because the required lateral force can be generated without approaching tire saturation, the closed-loop driver model can effortlessly suppress the crosswind disturbances, thereby exhibiting nearly identical macroscopic vehicle responses.



(a) Lateral acceleration **(b)** Yaw rate **(c)** Lateral displacement of CG

Figure 12: Effect of road adhesion coefficient on crosswind stability of truck.

When the road adhesion coefficient is relatively low, the lateral deviation and yaw motions of the truck undergo significant changes. At a road adhesion coefficient of 0.3, the box truck experiences sideslip. Influenced by the driving feedback control, the instant the crosswind dissipates further exacerbates the lateral deviation and yaw motions of the vehicle. The peak lateral acceleration reaches 0.19 g, the peak yaw rate hits 18.51°/s, and the peak lateral displacement of the center of mass is 0.74 m. However, the sideslip of the truck remains within a controllable range, and under the driver's feedback control, the vehicle gradually returns to its intended straight-line driving state.

4.4 Effect of Vehicle Load

Fig. 13 illustrates the influence of loading condition on the crosswind stability of the box truck, where the crosswind speed is 28.5 m/s, the vehicle speed is 80 km/h, the preview time is 1.4 s, and the road adhesion coefficient is 0.9. The variation in vehicle loading condition does not directly affect the magnitude of aerodynamic forces; however, it changes the center-of-gravity position and consequently influences the aerodynamic moments, particularly the aerodynamic yawing moment. Under the unladen condition, the aerodynamic yawing moment of the box truck is positive, causing the vehicle to yaw toward the upwind direction (i.e., the vehicle front turns to the right). The corresponding yaw-moment coefficient is 0.724, indicating a relatively strong resistance to crosswind-induced yaw disturbance. Under the laden condition, the center of gravity moves rearward by approximately 2 m, resulting in a negative aerodynamic yawing moment that causes the vehicle to yaw toward the downwind direction (i.e., the vehicle front turns to the left). The corresponding yaw-moment coefficient decreases to 0.113. Furthermore, the increased loading mass alters the center-of-gravity height and the aerodynamic moment arm, leading to a significant variation in the aerodynamic rolling moment acting on the vehicle. Therefore, box trucks under different loading conditions exhibit substantially different dynamic stability characteristics when subjected to crosswind disturbances. The unladen vehicle is particularly sensitive to crosswind effects and demonstrates poorer stability due to its lower mass, inertia, and tire vertical loads.

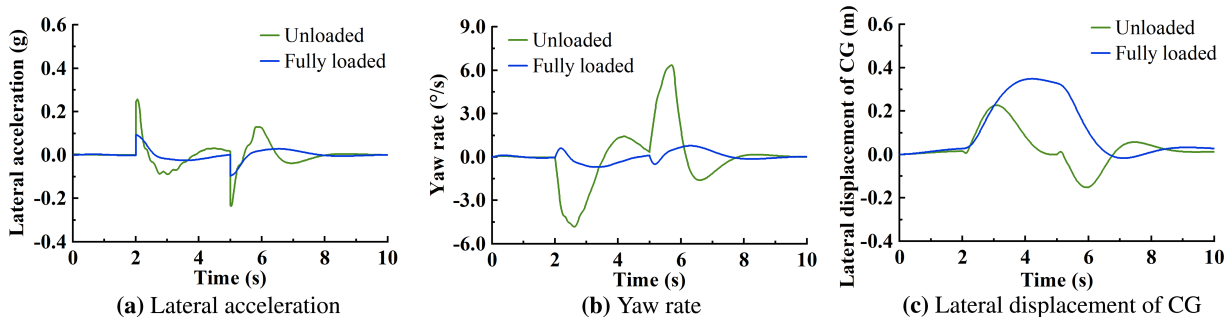


Figure 13: Effect of loading condition on the crosswind stability of the box truck.

Under the unladen condition, during and after the crosswind event, its lateral acceleration reaches positive peak values of 0.26 and 0.13 g, respectively, accompanied by significant negative fluctuations. The yaw rate plummets to −5°/s at the onset of the wind and rapidly rebounds to 6.6°/s after the wind dissipates. Simultaneously, the lateral displacement of the center of mass quickly turns negative and induces reverse oscillation, leading to prominent lateral deviation of the vehicle. In contrast, the laden state demonstrates superior wind-resistant stability and recovery capability. Its peak lateral acceleration is only about 0.16 g, and the peak yaw rate is as low as −1.2°/s, which smoothly recovers to near 0°/s after the wind subsides. Furthermore, none of the dynamic indicators exhibit drastic abrupt changes or obvious negative peaks. The fluctuation in the displacement of the center of mass remains minor, and no lateral deviation occurs throughout the entire process.

4.5 Effect of Preview Time

The driver's directional control process under crosswind conditions conforms to the preview-following theory. Taking the current vehicle state as a reference, the driver strives to minimize the tracking error when the vehicle reaches the forward preview point within the preview time. A shorter preview time and a smaller preview error reflect a higher level of driving proficiency. Therefore, the variation in preview time does not affect the lateral acceleration at the instant of crosswind impact; the peak lateral acceleration for all three preview times remains constant at 0.24 g. However, a longer preview time results in greater lateral deviation and yaw motions of the vehicle. When the preview times are 1.0 and 2.0 s, the peak yaw rates are 6.16°/s and 7.41°/s, respectively, while the peak lateral displacements are 0.17 and 0.51 m, respectively, as illustrated in Fig. 14.

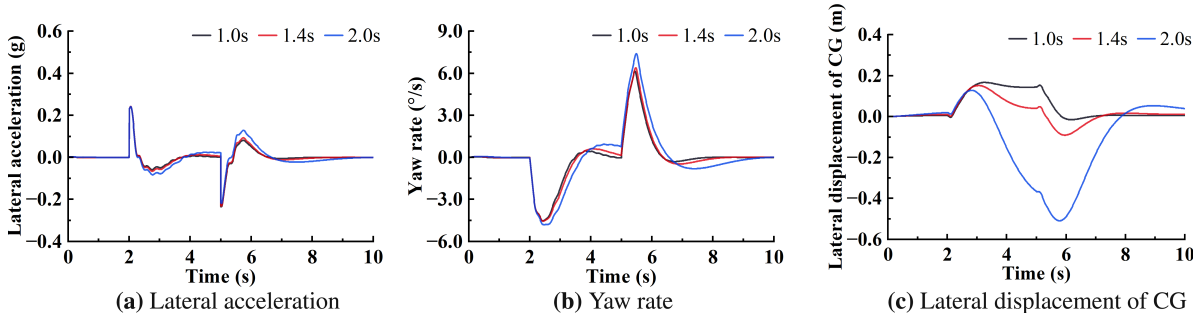


Figure 14: Effect of preview time on crosswind stability of truck.

4.6 Comprehensive Analysis of Coupled Physical Mechanisms

Although the independent effects of various factors on driving safety have been analyzed previously, wind-induced vehicle instability is fundamentally governed by the highly nonlinear coupled interactions among aerodynamic loads, vehicle payloads, tire dynamics, and driver control.

From the perspective of vehicle dynamics, the influence of loading condition on crosswind stability cannot be explained solely by the change in center-of-gravity height. In the TruckSim model used in this study, the center-of-gravity heights under the unladen and laden conditions are 1175 and 1935 mm, respectively, indicating that the center of gravity is elevated after loading. Compared with the unladen condition, the center of gravity of the fully loaded vehicle also shifts rearward by approximately 2 m.

Although a higher center of gravity increases the lever arm associated with lateral load transfer and is therefore unfavorable for rollover stability when considered independently, loading simultaneously increases the total vehicle mass, moments of inertia, and vertical tire loads. Under the same or similar aerodynamic side force and rolling moment, the increased vehicle mass and inertia reduce lateral acceleration and yaw responses, while the higher vertical tire loads improve the vehicle's ability to resist lateral disturbances.

Furthermore, the elevated center-of-gravity position and the rearward shift of the center of gravity modify the aerodynamic moment characteristics acting at the vehicle reference point. The resulting reduction in aerodynamic rolling and yawing moments under the laden condition decreases the risk of rollover and sideslip under strong crosswind conditions, respectively. The results of this study indicate that, within the investigated range of operating conditions, these stabilizing effects outweigh the adverse influence caused by the increased center-of-gravity height. Consequently, the laden vehicle exhibits better overall crosswind stability than the unladen vehicle.

In contrast, although the unladen vehicle has a lower center of gravity, its lower total mass and moments of inertia make it more susceptible to larger lateral accelerations and yaw responses under the same crosswind-induced aerodynamic loads. Meanwhile, the lower vertical tire loads cause the vehicle to approach the available lateral tire-force limit more readily under low-adhesion road conditions. Therefore, the unladen vehicle is more sensitive to the coupled effects of strong crosswinds and low road adhesion, exhibiting more pronounced tendencies toward lateral deviation, sideslip, and instability.

From the perspective of lateral dynamics, the extreme aerodynamic lateral force demands exceptionally high tire cornering forces. When this high aerodynamic demand is coupled with a reduced road adhesion coefficient, the tire's friction ellipse is severely compressed. The superposition of these two phenomena—the reduction of vertical load and the shrinkage of the friction ellipse—forces the tires to rapidly exceed their linear operating limits and plunge into the nonlinear saturation region.

Once the tires reach saturation, the closed-loop coupling with driver control deteriorates sharply. The steering interventions executed by the MacAdam preview control model can no longer induce a proportional increase in tire lateral force. This saturation leads to a severe phase lag between the driver's steering input and the actual yaw response of the vehicle, which in turn triggers excessively amplified lateral deviation and violent, irrecoverable yaw rate oscillations. Therefore, the critical driving risk on cross-sea bridges precisely manifests at the intersection of these coupling effects: when extreme aerodynamic loads overwhelm the reduced tire-road friction limits of a lightly loaded vehicle, steering corrections from either a human driver or an autonomous system become dynamically and completely ineffective.

Delving deeper into this nonlinear coupling mechanism, it is evident that under milder environmental conditions, the aerodynamic lateral force and rolling moment are relatively small. In such cases, the lateral load transfer of the vehicle is negligible, and the high-adhesion road surface provides a broad boundary for the tire friction ellipse. The tires operate stably within the linear region of their cornering stiffness. At

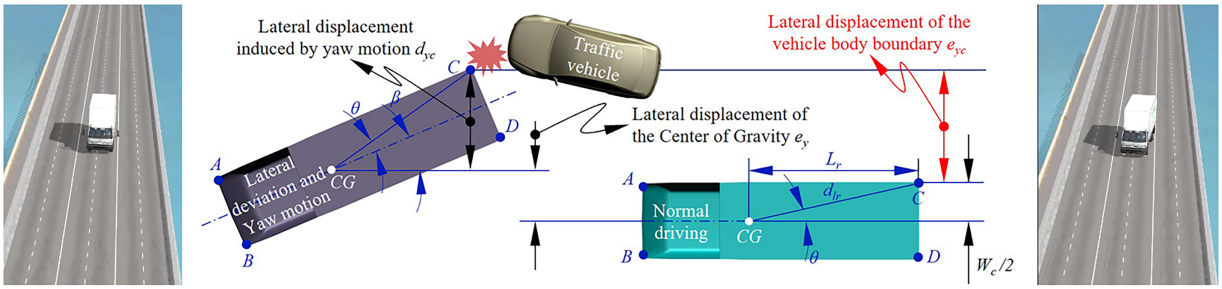
this point, the preview control model only needs to apply minor steering inputs to obtain proportional lateral force feedback; the vehicle can swiftly correct its trajectory with minimal phase lag, and the overall system exhibits extremely high robustness. Conversely, when a "strong crosswind" encounters a "slippery road surface," the system enters the most adverse coupled scenario. The massive aerodynamic lateral thrust brutally deprives the windward tires of their grip, while the low-adhesion road fundamentally locks the available friction limit. Consequently, abrupt and severe changes occur in lateral displacement and yaw rate, the tires instantly reach complete saturation, and the risks of sideslip and even rollover are drastically magnified.

The severity of the aforementioned dynamic deterioration is acutely amplified by the longitudinal traveling speed of the vehicle. An increase in vehicle speed not only raises the relative airflow velocity around the vehicle body, significantly elevating the absolute magnitude of the aerodynamic loads; more lethally, high-speed driving substantially increases the demand for tire longitudinal force to maintain longitudinal motion. According to the friction ellipse principle, the occupation by the longitudinal force further encroaches upon the already scarce lateral adhesion limit. In addition, high vehicle speeds drastically compress the driver's reaction window within the preview time. Therefore, reducing vehicle speed serves as the most direct and effective control intervention to break this vicious cycle of "aerodynamics-dynamics-driver feedback."

5 Prediction of Wind-Induced Driving Safety for Box Trucks

5.1 Evaluation Method for Wind-Induced Driving Safety

The wind-induced driving safety of trucks on bridges is evaluated using three criteria: lateral deviation, sideslip, and rollover. The safety evaluation of lateral deviation comprehensively accounts for both the lateral motion of the center of mass and the yaw motion of the vehicle body. Therefore, it is more scientifically rigorous to evaluate this using the maximum lateral displacement of the vehicle's body contour boundary. Taking the scenario with a crosswind speed of 28.5 m/s, a vehicle speed of 80 km/h, and a road adhesion coefficient of 0.9 as an example: although the lateral displacement of the center of mass is smaller in the unladen state, its yaw angle is significantly larger. Consequently, the lateral displacement of its contour boundary points is greater compared to the laden state. An excessive lateral displacement of the vehicle body contour may cause the truck to drift out of its lane, potentially leading to collisions with vehicles in adjacent lanes or the auxiliary structures of the bridge, as illustrated in Fig. 15a,c.



(a) Fully laden limit state

(b) Geometric relationship

(c) Unladen limit state

Figure 15: Calculation method of lateral movement for box truck.

Fig. 15b provides a schematic diagram for calculating the lateral displacement e_{yc} of the outermost contour point C under the lateral deviation state. The geometric and kinematic variables required to determine this displacement are calculated using Eqs. (4) and (5), whereas the actual safety criterion for

lateral deviation is strictly defined by the inequality boundary presented in Eq. (4). The calculation methods for the other contour boundary points are similar and are omitted here for brevity due to space constraints.

The sideslip and rollover mechanisms of the vehicle can be elucidated through the friction ellipse theory and the lateral load transfer mechanism, respectively. Based on the friction ellipse principle, the total friction limit provided by the tires on a specific road surface is a constant value. As high vehicle speeds lead to a continuous increase in the longitudinal tire force, the upper limit of the available lateral force to resist disturbances will correspondingly decrease. Under these conditions, the occurrence of crosswind disturbances can easily breach the lateral adhesion limit, thereby inducing vehicle sideslip [33]. The condition for avoiding sideslip is given in Eq. (6). On the other hand, severe crosswinds trigger drastic lateral load transfer across the vehicle body. When the vertical contact force of the windward tires suddenly plummets to zero within an extremely short period, meaning the Lateral Load Transfer Ratio (LTR) reaches its physical limit of 1 ($LTR = 1$), the vehicle loses its roll equilibrium and subsequently faces a critical risk of rollover [34].

$$e_{yc} = d_{yc} + e_y - \frac{W_C}{2} \le \frac{W_R - W_C}{2}$$
$$d_{yc} = d_{lr} \times \sin(\theta + \beta) \tag{4}$$
$$d_{lr} = \sqrt{\left(\frac{W_C}{2}\right)^2 + (L_r)^2}$$
$$\theta = \arcsin\left(\frac{1}{2} W_C / d_{lr}\right) \tag{5}$$
$$F_x^2 + F_y^2 \le (\mu F_z)^2 \tag{6}$$

In the equation: d_{yc} represents the lateral distance from the contour point C to the center of gravity (CG) following the lateral deviation; e_y denotes the lateral displacement of the CG; W_C and W_R represent the width of the vehicle body and the width of the road (or lane), respectively; d_{lr} is the distance between the CG and the contour point C; θ is the geometric angle between the line connecting the CG to point C and the vehicle's longitudinal axis; β signifies the yaw angle; F_x, F_y and F_z represent the longitudinal force, lateral force, and vertical load of the tire, respectively, and μ denotes the road adhesion coefficient, the variations of which under different conditions are illustrated in Fig. 16; and L_r is the longitudinal distance from the CG to the rear end of the vehicle.

5.2 Prediction Model and Methodology

Based on the crosswind stability analysis model, a dynamic response dataset for the box truck under the influence of complex multiple variables was acquired, comprising a total of 2764 data records. This dataset encompasses several critical variables affecting wind-induced driving safety, including input variables such as crosswind speed, vehicle speed, vehicle payload, road adhesion coefficient, and preview time, as well as output variables corresponding to lateral deviation, sideslip, and rollover accidents. The dataset was normalized to eliminate dimensional effects. The eXtreme Gradient Boosting (XGBoost) algorithm was employed as the core machine learning model to construct a wind-induced driving safety assessment model, aiming to predict the driving states and safe vehicle speeds of the truck on the bridge under varying environmental factors, as illustrated in Fig. 17. This model demonstrates excellent performance in predicting driving safety risks [35]. Its objective function, $obj(\theta)$, is determined by Eqs. (7) and (8), consisting of a loss function $L(y, \hat{y})$ and a regularization term $\Omega(f)$ related to the complexity of the decision tree.

$$\text{obj}(\theta) = \sum_{i=1}^{n} L(y_i, \hat{y}_i) + \sum_{k=1}^{K} \Omega(f_k) \tag{7}$$

$$\Omega(f) = \gamma T + \frac{1}{2}\lambda \|w\|^2 \tag{8}$$

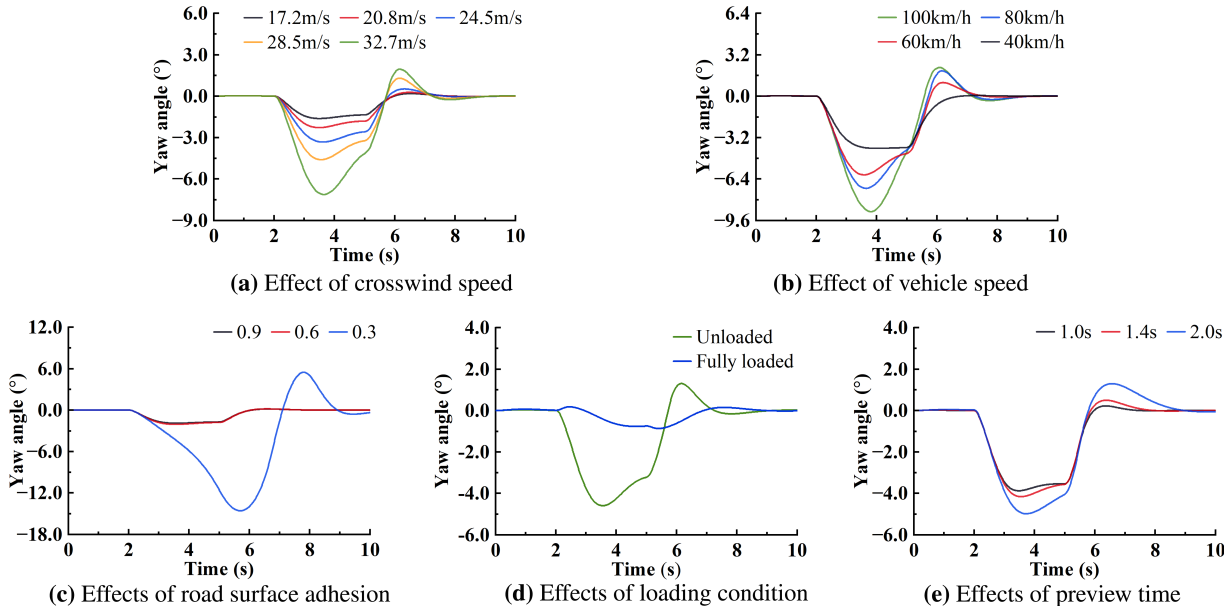


Figure 16: Yaw-angle responses of the box truck under different operating conditions.

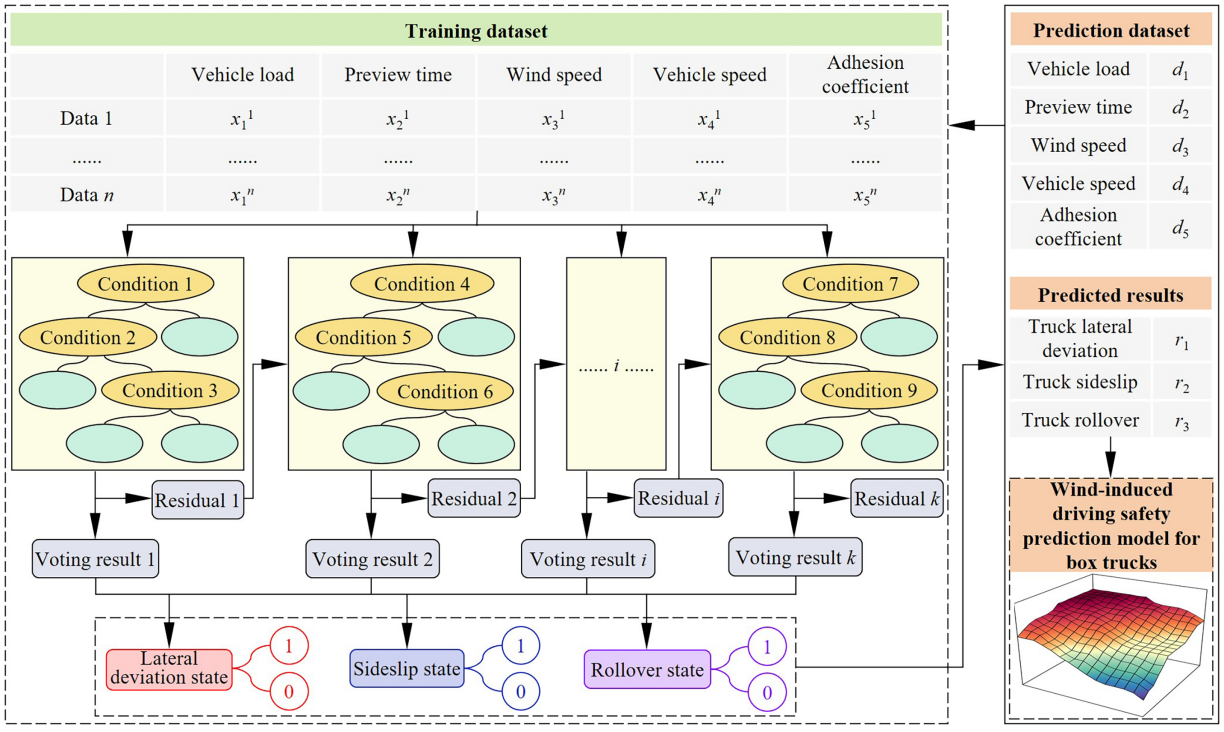


Figure 17: Extreme gradient boosting algorithm.

In the equation: y_i represents the ground truth (actual value); $\hat{y}_i$ denotes the predicted value; the loss function quantifies the discrepancy between the model's predictions and the ground truth; K is the total number of decision trees; f_k corresponds to the k decision tree; γ and λ serve as regularization parameters; T indicates the number of leaf nodes; and w represents the leaf weights.

Each decision tree is optimized by applying a second-order Taylor expansion, as shown in Eq. (9). By eliminating the constant terms and expanding the regularization term, Eqs. (10) and (11) are derived, respectively, which ultimately yields the final optimization objective function expressed in Eq. (12).

$$\mathrm{obj}^{(t)} \approx \sum_{i=1}^{m}\left[L\left(y_i, \hat{y}_i^{(t-1)}\right) + g_i f_t\left(x_i\right) + \frac{1}{2} h_i f_t^2\left(x_i\right)\right] + \sum_{k=1}^{t-1} \Omega\left(f_k\right) + \Omega\left(f_t\right) \tag{9}$$

$$\mathrm{obj}^{(t)} \approx \sum_{i=1}^{m}\left[g_i f_t\left(x_i\right) + \frac{1}{2} h_i f_t^2\left(x_i\right)\right] + \Omega\left(f_t\right) \tag{10}$$

$$\mathrm{obj}^{(t)} \approx \sum_{i=1}^{m}\left[g_i f_t\left(x_i\right) + \frac{1}{2} h_i f_t^2\left(x_i\right)\right] + \gamma T + \frac{1}{2}\lambda \|w\|^2 \tag{11}$$

$$\mathrm{obj}^{(t)} = -\frac{1}{2}\sum_{i=1}^{T}\left(\frac{G_i^2}{H_i + \lambda}\right) + \gamma T \tag{12}$$

In the equation: g_i and h_i represent the first and second order derivatives (i.e., gradient and Hessian) of the loss function, respectively; G_i and H_i are determined by Eq. (13); and I_j denotes the set of sample instances contained in the j leaf node.

$$G_i = \sum_{i \in I_j} g_i\,,\; H_i = \sum_{i \in I_j} h_i \tag{13}$$

Regarding the construction of the model tree, the optimal splitting point is selected based on Eq. (8). If the value of Gain calculated in Eq. (14) is greater than 0, a split is executed; otherwise, it is rejected. The splitting process is terminated when the tree reaches its maximum depth or when the number of leaf nodes falls below a specified threshold.

$$\mathrm{Gain} = \mathrm{obj}_{\mathrm{L+R}} - \left(\mathrm{obj}_{\mathrm{L}} + \mathrm{obj}_{\mathrm{R}}\right) = \frac{1}{2}\left[\frac{G_L^2}{H_L + \lambda} + \frac{G_R^2}{H_R + \lambda} - \frac{\left(G_L + G_R\right)^2}{H_L + H_R + \lambda}\right] - \gamma \tag{14}$$

To rigorously quantify the aforementioned heuristic dynamic adjustment process of safe vehicle speeds, this study introduces the theory of actionable recourse for black-box machine learning models [36] and the discrete iterative descent algorithm [37], thereby providing a comprehensive mathematical description of this prediction process. In the context of this paper, actionable recourse refers to determining the minimum necessary adjustment to the actionable input feature (i.e., reducing the driving speed) required to transition the model's output from a critical risk state across the decision boundary into the safe domain.

Extracting the key input variables of this study, the real-time meteorological conditions and the inherent vehicle state are defined as the static environmental constraint vector $E = \left[v_m, m, \mu, t_p\right]^T$. The trained XGBoost model is abstracted as a high-dimensional nonlinear mapping function F_{XGB}.

Let the current initial driving speed of the vehicle be v_0. The system first inputs E and v_0 into the model to estimate the initial-state risk probabilities (P_0) for lateral deviation, sideslip, and rollover:

$$P_0 = F_{XGB}\left(E, v_0\right) = \left[P_{dev,0}, P_{slip,0}, P_{roll,0}\right] \tag{15}$$

where $P_{dev,0}$ denotes the probability of lateral-deviation instability in the initial state, $P_{slip,0}$ denotes the probability of sideslip instability in the initial state, and $P_{roll,0}$ denotes the probability of rollover instability in the initial state.

The joint risk index is defined as $R_k = \max(P_{dev,k}, P_{slip,k}, P_{roll,k})$. The safety decision tolerance threshold of the system is set to τ (the classification threshold in this paper is $\tau = 0.5$). If $R_0 < \tau$, the initial state is determined to be safe, the target safe speed $V_{safe} = v_0$, and the algorithm terminates. If $R_0 \geq \tau$, the iterative speed adjustment mechanism is triggered.

According to the physical priors of vehicle dynamics, the instability risk is monotonically non-decreasing with vehicle speed. Therefore, by setting a fixed deceleration step size $\Delta v = 1$ km/h, the system constructs a unidirectional discrete iterative descent sequence. The new vehicle speed v_k generated in the k-th iteration and the corresponding re-evaluated risk P_k satisfy the following recurrence relation:

$$\begin{aligned} v_k &= v_{k-1} - \Delta v \ (k = 1, 2, \cdots) \\ P_K &= F_{XGB}(E, v_k) \end{aligned} \tag{16}$$

This process does not require calculating the missing gradients due to the non-differentiability of the tree model; it relies solely on the forward propagation of the model to conduct multi-round re-evaluations of the safety state.

The iterative adjustment process continues until an evaluation result satisfying the safety constraint condition appears for the first time in the sequence. Mathematically, the system searches for the minimum number of iteration steps K that satisfies the safety threshold:

$$K = \min\{k \in \mathbb{N}^+ | F_{XGB}(E, v_k) < \tau\} \tag{17}$$

When this condition is triggered, the iteration terminates. The final safe driving speed determined at this time is $V_{safe} = v_k$. Through this sequence of equations, the proposed model strictly transforms qualitative "speed adjustment suggestions" into a mathematically programmable optimization algorithm ready for deployment.

Taking into account the actual speed limit regulations for cross-sea bridges, the maximum vehicle speed is typically restricted to 80 km/h. Therefore, the upper limit for the safe speed is set at 80 km/h. In high-wind environments, from the dual perspectives of traffic efficiency and safety, it is recommended to suspend traffic when the calculated safe speed falls below 20 km/h; consequently, the safe speed under such conditions is defined as 0. Based on the aforementioned rules and in conjunction with the safe speed prediction model developed in this study, the safe speed fitting function for cross-sea bridges is constructed as follows:

$$V_{safe}(v, \mu) = \begin{cases} 80 & f(v, \mu) \geq 80\text{km/h} \\ f(v, \mu) & 20\text{km/h} \leq f(v, \mu) < 80\text{km/h} \\ 0 & f(v, \mu) < 20\text{km/h} \end{cases} \tag{18}$$

$$f(v, \mu) = P_1 + P_2 v + P_3 \mu + P_4 v^2 + P_5 v\mu + P_6 \mu^2 + P_7 v^3 + P_8 v^2 \mu + P_9 v\mu^2 + P_{10} \mu^3 \tag{19}$$

where $f(v, \mu)$ denotes the predicted safe vehicle speed, v denotes the crosswind speed, and μ denotes the dimensionless road adhesion coefficient. It should be noted that the polynomial fitting of the safe vehicle speed was performed directly using the original physical values of the crosswind speed and road adhesion coefficient. The coefficients P_i are dimensional fitting coefficients with units corresponding to the respective polynomial terms, as listed in Table 2.

Table 2: Specific values of P_i.

	Unladen	Fully Laden	Unit
P_1	−145.60	432.18	km/h
P_2	25.20	−43.50	(km/h)/(m/s)
P_3	119.48	−337.16	km/h
P_4	−1.28	1.36	$(km/h)/(m/s)^2$
P_5	11.03	71.45	(km/h)/(m/s)
P_6	−232.16	−1152.38	km/h
P_7	0.02	−0.01	$(km/h)/(m/s)^3$
P_8	−0.72	−1.72	$(km/h)/(m/s)^2$
P_9	18.31	27.31	(km/h)/(m/s)
P_{10}	−144.87	152.55	km/h

For the unladen box truck, the regression analysis yielded a coefficient of determination (R^2) as high as 0.9875 and a root mean square error (RMSE) of 1.5811 km/h. Similarly, for the fully laden state, the regression analysis achieved an R^2 value of 0.9601 and an RMSE of 2.7674 km/h. The obtained R^2 and RMSE values indicate that the polynomial surfaces provide a good representation of the predicted safe-speed data within the investigated parameter domain.

In real-world driving environments on cross-sea bridges under strong crosswinds, extreme hazardous states (especially rollovers) are inherently low-probability events. To accurately reflect this physical reality, the simulation dataset constructed in this study, which comprises 2764 valid records, exhibits an objective characteristic of class imbalance.

The risk prediction task in this study is formulated as a multi-label classification problem rather than a mutually exclusive multi-class classification problem. Each vehicle operating scenario is associated with three independent binary risk labels corresponding to lateral deviation, sideslip, and rollover. When a given scenario simultaneously satisfies multiple instability criteria, multiple positive labels may be assigned to that scenario. As shown in Table 3, the counts and proportions of positive and negative samples for the three risk states—lateral deviation, sideslip, and rollover—are detailed in the dataset. It can be observed that lateral deviation, being the most easily occurring instability state, has a relatively high proportion of positive samples (58.0%). In contrast, rollover, as an extreme instability state, accounts for an extremely small number of positive samples (only 0.3%). This severe class imbalance phenomenon imposes highly demanding requirements on the machine learning model's capability to identify minority classes. Therefore, in the subsequent model performance evaluation, rather than relying solely on a single accuracy metric, this study specifically introduces evaluation metrics that are more robust to imbalanced data, such as the Macro-F1, and Hamming Loss, thereby ensuring the scientific rigor and objectivity of the evaluation results.

Table 3: Statistical summary of class distribution in the driving safety dataset.

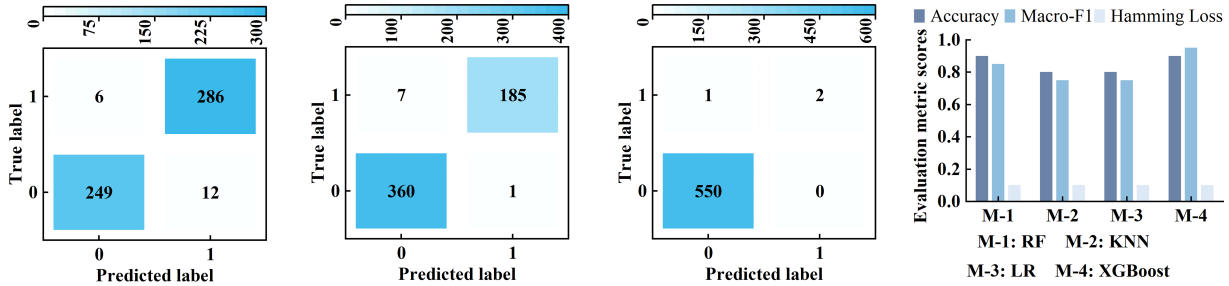
Risk State	Total Samples	Positive Samples (Occurred = 1)	Negative Samples (Not Occurred = 0)	Proportion of Positive Samples (%)
Lateral deviation	2764	1602	1162	58.0%
Sideslip	2764	1114	1650	40.3%
Rollover	2764	8	2756	0.3%

The dataset was divided into a training set and a test set at a ratio of 8:2. The training set was used for model training and hyperparameter tuning, while the test set was used to evaluate the predictive performance of the trained model. During data partitioning, particular attention was paid to maintaining broadly consistent distributions of the input variables between the training and test sets.

The hyperparameters of the XGBoost model were optimized using a randomized grid-search strategy. Candidate hyperparameter combinations were randomly sampled from predefined search ranges, and models with different parameter configurations were trained separately. The optimized hyperparameter settings were then determined by comparing their predictive performance. Considering the limited dataset size, 5-fold cross-validation was further employed. Specifically, the data were divided into five subsets of approximately equal size. In each iteration, one subset was used as the validation set and the remaining four subsets were used for training. This procedure was repeated five times, and the average performance across the five folds was used to evaluate the stability of the model under different data partitions. The primary parameters were ultimately determined as follows: the base classifier is gbtree, the number of iterations is 300, the learning rate is 0.1, the maximum depth of the decision tree is 5, the minimum child weight is 2, the minimum loss reduction required for a split is 0.1, the feature subsampling ratio is 0.8, and the regularization term on weights is 0.5. All other parameters were kept at their default values.

5.3 Confusion Matrix and Performance Analysis

Fig. 18a–c illustrates the confusion matrices generated by the predictive model, while Table 4 details the corresponding numerical values for each predicted risk state. To rigorously evaluate the model's performance, metrics including accuracy, precision, recall, and the F1-score were calculated based on these confusion matrices, as presented in Table 5. The results demonstrate that the model achieves exceptionally high precision and recall (both exceeding 95%) for the lateral deviation and sideslip states, which possess larger sample sizes. It should be noted that, for the rollover category, the test set contained only three positive samples, of which two were correctly identified and one was missed. The corresponding Precision and Recall values were relatively favorable. Although no false-positive rollover predictions occurred in this particular test split, the extremely limited number of positive samples prevents a definitive assessment of the model's generalization capability for rollover events. The overall model performance was further evaluated using exact-match accuracy, Macro-F1, and Hamming Loss.



(a) Confusion matrix of lateral deviation state **(b)** Confusion matrix of sideslip state **(c)** Confusion matrix of rollover state **(d)** Model comparison

Figure 18: Performance evaluation of predictive model.

Table 4: Confusion matrix for the prediction of each risk state.

Risk State	Actual Label	Predicted as 0 (Not Occurred)	Predicted as 1 (Occurred)
Lateral deviation	Actual 0	249	12
	Actual 1	6	286
Sideslip	Actual 0	360	1
	Actual 1	7	185
Rollover	Actual 0	550	0
	Actual 1	1	2

Table 5: Label-specific predictive performance of the XGBoost model.

Risk State	Accuracy	Precision	Recall	F1-Score
Lateral deviation	96.75%	95.97%	97.95%	96.95%
Sideslip	98.55%	99.46%	96.35%	97.88%
Rollover	99.82%	100.00%	66.67%	80.00%

The proposed model exhibits strong classification capability and achieves satisfactory overall classification performance on the current test set. The prediction model achieved an exact-match accuracy of 95.7% on the test set, where a sample was considered correctly predicted only when all three predicted labels exactly matched their corresponding ground-truth labels. The Macro-F1 score is 0.916, and the Hamming Loss is 0.016. Common models, including Random Forest (RF), K-Nearest Neighbors (KNN), and Logistic Regression (LR), were selected for comparison with the XGBoost algorithm, as shown in Fig. 18d. Among the compared models, XGBoost achieved the highest overall accuracy and Macro-F1 score and the lowest Hamming Loss on the current dataset, indicating better overall predictive performance under the present evaluation framework.

Based on a single independent test set obtained from a random 8:2 split, the XGBoost model achieved an exact-match accuracy of 95.7%, a Macro-F1 score of 0.916, and a Hamming Loss of 0.016. These results reflect the predictive performance of the model under the current data partition. It should be noted that the exact-match accuracy of 95.7% represents a point estimate from a single random split and may therefore be influenced by the specific sample allocation and class distribution.

To further evaluate the internal stability of the selected model on the current simulation dataset and its sensitivity to different data partitions, 5-fold cross-validation was performed on the complete dataset containing 2764 records. In each fold, one subset was used as the validation set, while the remaining four subsets were used for model training. The Accuracy obtained for each validation fold was recorded, and the mean and standard deviation across the five folds were subsequently calculated as descriptive statistics of model-performance stability. The variation in performance across different validation folds was used primarily to assess the internal robustness of the model and should not be interpreted as an independent estimate of its generalization capability under real-world conditions.

As shown in Table 6, the XGBoost model exhibited generally stable predictive performance across the five validation folds, with a mean accuracy of 94.68%. The relatively limited variation in performance among the folds indicates that the model maintained consistent predictive performance under different internal

partitions of the current simulation dataset. Compared with the other models included in the comparison, XGBoost also achieved the highest mean accuracy in the present cross-validation analysis.

Table 6: Fold-wise accuracy and descriptive statistics of the compared models under 5-fold cross-validation.

Model	Fold 1	Fold 2	Fold 3	Fold 4	Fold 5	Average Accuracy	Standard Deviation
M1: Random Forest	0.9024	0.9367	0.9385	0.9186	0.9312	0.9255	0.0151
M2: KNN	0.7866	0.7920	0.7975	0.7685	0.7464	0.7782	0.0208
M3: Logistic Regression	0.7794	0.8047	0.8174	0.7939	0.8188	0.8028	0.0166
M4: XGBoost	0.9458	0.9476	0.9494	0.9512	0.9402	0.9468	0.0042

In summary, the 5-fold cross-validation results indicate that the selected XGBoost model maintained relatively stable predictive performance across different partitions of the current simulation dataset, providing supplementary evidence of the model's internal robustness. Furthermore, the detailed confusion matrix and advanced evaluation metrics (Macro-F1 and Hamming Loss) provide a complementary assessment of the model's multi-label prediction performance from an overall perspective. However, considering the extremely limited number of positive rollover samples, the model's capability in predicting extreme minority-class events still requires further validation with a larger number of samples. According to the feature importance analysis results, among the factors affecting wind-induced driving safety, the vehicle payload state has the greatest impact, followed by the road adhesion coefficient, crosswind speed, and vehicle speed. By comparison, the influence of preview time is relatively minor; however, this does not imply that the role of driver preview time in safe driving can be ignored.

To break the "black-box" nature of machine learning and enhance the engineering significance of this study, a comprehensive physical connection must be established among the CFD flow field results, vehicle dynamics mechanisms, and machine learning predictions.

First, at the CFD level, although the bridge barriers provide a certain shielding effect, the severe aerodynamic lateral force and rolling moment generated by extreme crosswinds constitute the primary external disturbances. From the perspective of vehicle dynamics, these extreme aerodynamic moments can induce severe lateral load transfer. This effect is particularly pronounced under unladen conditions, where the lower total vehicle mass, moments of inertia, and vertical tire loads make the vehicle more sensitive to strong crosswind disturbances, resulting in larger lateral and yaw dynamic responses. This load transfer drastically reduces the vertical load on the windward tires. When this phenomenon is coupled with a reduced road adhesion coefficient, the tire's friction ellipse is severely compressed, forcing the tires to abruptly breach their linear operating limits and enter the nonlinear saturation region, ultimately triggering macroscopic vehicle instability phenomena such as sideslip and rollover.

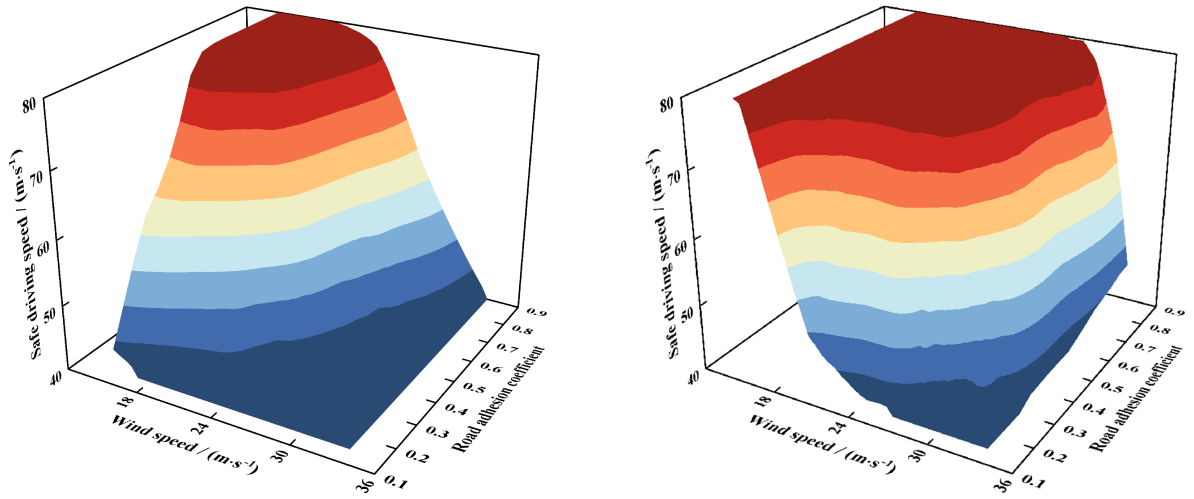
Notably, the feature importance analysis of the XGBoost model reveals that "vehicle payload state," "road adhesion coefficient," and "crosswind speed" occupy the highest decision weights. The feature-importance ranking and classification results show good consistency with the aforementioned vehicle-dynamics mechanisms, indicating that the risk patterns learned by the model reflect the underlying physical mechanisms to some extent. This consistency between the data-driven predictions and the underlying fluid–multibody dynamics mechanisms provides a degree of physical interpretability for the model predictions.

6 Conceptual Framework for Smart Bridge Management

A wide variety of vehicle types travel on cross-sea bridges, commonly including passenger cars, box trucks, and container trucks. Among these vehicles, wind engineering literature widely recognizes the box truck as one of the most susceptible models under strong crosswind conditions, exhibiting the poorest stability. This high sensitivity is mainly attributed to the large lateral projected area of the box-shaped body and the resulting substantial aerodynamic side force and overturning moment [38]. In addition, the loading condition further influences the vehicle's dynamic response to crosswinds by simultaneously altering the total vehicle mass, moments of inertia, vertical tire loads, and center-of-gravity position. Therefore, utilizing the box truck as the reference vehicle model for traffic safety management across the entire bridge offers stronger practical operability and guiding significance for enhancing traffic safety guarantees on cross-sea bridges.

6.1 Prediction of Safe Driving Speed

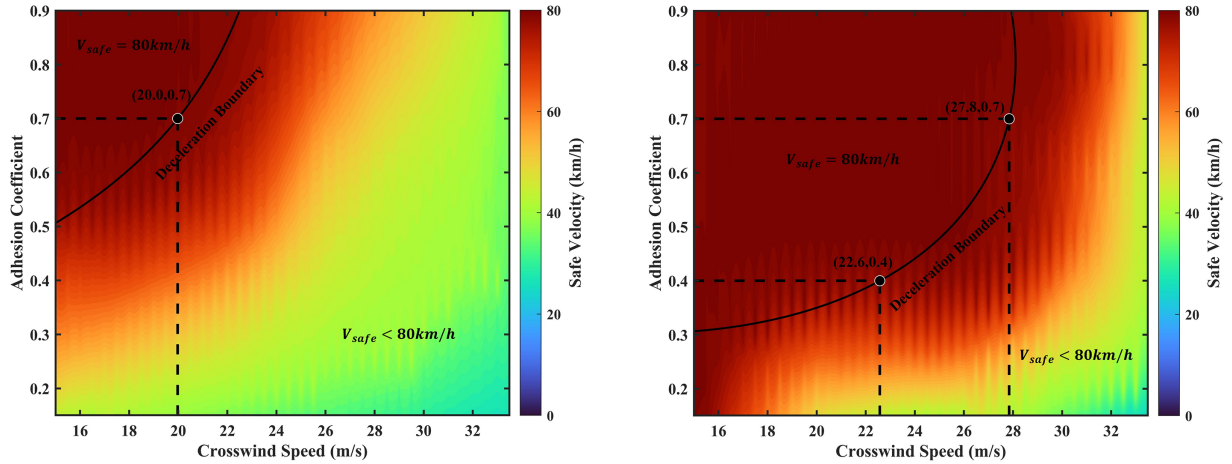
Based on the prediction model, a safe vehicle speed prediction model for box trucks under different combinations of input parameters can be derived, providing a scientific basis for the intelligent management and control of wind-induced driving safety on cross-sea bridges. The paper outputs the safe vehicle speed prediction models under different crosswind speeds and road adhesion conditions, as shown in Fig. 19, where the preview time is set to 1.4 s. Under the premise of ensuring that no lateral deviation, sideslip, or rollover occurs, the safe vehicle speed decreases as the crosswind speed increases and as the road adhesion capacity decreases. Compared to the fully laden state, the safe vehicle speed in the unladen state is significantly lower.



(a) Unloaded state **(b)** Fully loaded

Figure 19: Prediction model of safe speed.

Based on the safe vehicle speed prediction model shown in Fig. 19, the safe driving speeds of trucks on the bridge under any working condition within the variation ranges of crosswind speed and road adhesion coefficient can be obtained. Fig. 20 illustrates the driving safety domains of the vehicle, which are plotted against crosswind speed and road adhesion coefficient using fitting functions based on the predicted safe vehicle speeds. The black line in this safety domain represents the "speed reduction boundary"; the upper-left side of the boundary is the safe region, while the lower-right side is the dynamic speed reduction region. A comparative analysis of the safety domain characteristics under unladen and fully laden states clearly reveals the decisive influence of the vehicle payload state on lateral wind-resistant stability.



(a) Unladen safety domain **(b)** Fully loaded safety domain

Figure 20: Driving safety domains under unladen and fully loaded conditions.

In the unladen state (Fig. 20a), the speed reduction boundary shifts towards the upper left of the parameter space as a whole, and the area of the absolute safe region shrinks significantly. This indicates that the unladen vehicle, due to its lighter overall mass, exhibits extremely high sensitivity to the coupled excitation of "strong crosswind-low adhesion." Specifically, extracting the intersection points from the figure reveals that when the road surface is in a good adhesion condition—such as a constant road adhesion coefficient of 0.7—the critical crosswind speed at which the safe vehicle speed of the unladen truck drops below 80 km/h is only 20.0 m/s. This implies that even with sufficient road anti-skid capability, the aerodynamic moment induced by strong crosswinds will still force the unladen vehicle to enter the speed reduction region prematurely.

Conversely, in the fully laden state (Fig. 20b), the increase in overall mass substantially enhances the vehicle's anti-overturning capability, significantly expanding its safe driving domain towards the lower right. Horizontally comparing the influence of payload states, under equally good adhesion conditions, the limit crosswind speed that the fully laden vehicle can withstand is relaxed to 27.8 m/s, representing a substantial increase of 39.0% compared to the unladen state before a mandatory speed reduction is required. Furthermore, vertically comparing the deterioration effect of the road environment, the attenuation of road adhesion conditions exerts a significant weakening effect on the critical crosswind speed. As shown in the figure, for the fully laden truck, when the adhesion coefficient drops from 0.7 to a moderately slippery state of 0.4, its safety critical point slides towards the upper left along the speed reduction boundary. The maximum allowable wind resistance threshold plummets from 27.8 to 22.6 m/s, marking an 18.7% drop in wind-resistant performance. This quantified intersection offset pattern clearly demonstrates that the attenuation of road friction significantly amplifies the threat of strong winds to driving safety by a proportion of nearly 20%. Therefore, under the coupled conditions of "strong wind-low adhesion," more conservative dynamic speed limit strategies must be adopted to guarantee the operational safety of bridge traffic.

Therefore, in the traffic management of cross-sea bridges under strong wind climates, personalized traffic control strategies can be formulated for trucks on the bridge based on the monitored crosswind speeds at the deck height and the road adhesion capacity. This holds significant engineering importance for improving the wind-induced driving safety capability of trucks on bridges in strong wind environments.

6.2 Vision for Smart Bridge Management and Control

To address the future requirements of intelligent infrastructure development and refined traffic management for cross-sea bridges, and to further enhance the resilience of bridge traffic safety under extreme wind conditions, this study proposes a forward-looking conceptual framework for intelligent dynamic traffic management of box trucks in strong-wind bridge environments based on the previously developed wind-induced driving safety prediction model (Fig. 21). This idealized control system forms a closed-loop comprising four core logical modules: the input layer, the calculation layer, the decision layer, and the execution layer. In the future smart bridge application vision, this control strategy aims to achieve real-time fusion of multi-source heterogeneous information from the bridge deck micro-meteorological monitoring network and entering vehicles, which is synchronously fed into the cloud-based XGBoost risk prediction model to online compute the transient instability (lateral deviation, sideslip, and rollover) risk probabilities of specific vehicles under current environments. Based on the risk probabilities predicted by the model, the system integrates the vehicle-instability risk assessment with the corresponding safe vehicle speed to generate traffic-control instructions. According to the relationship between the current vehicle speed and the predicted safe vehicle speed, the management framework classifies the traffic-control state into three levels: normal operation, speed-limit intervention, and traffic suspension.

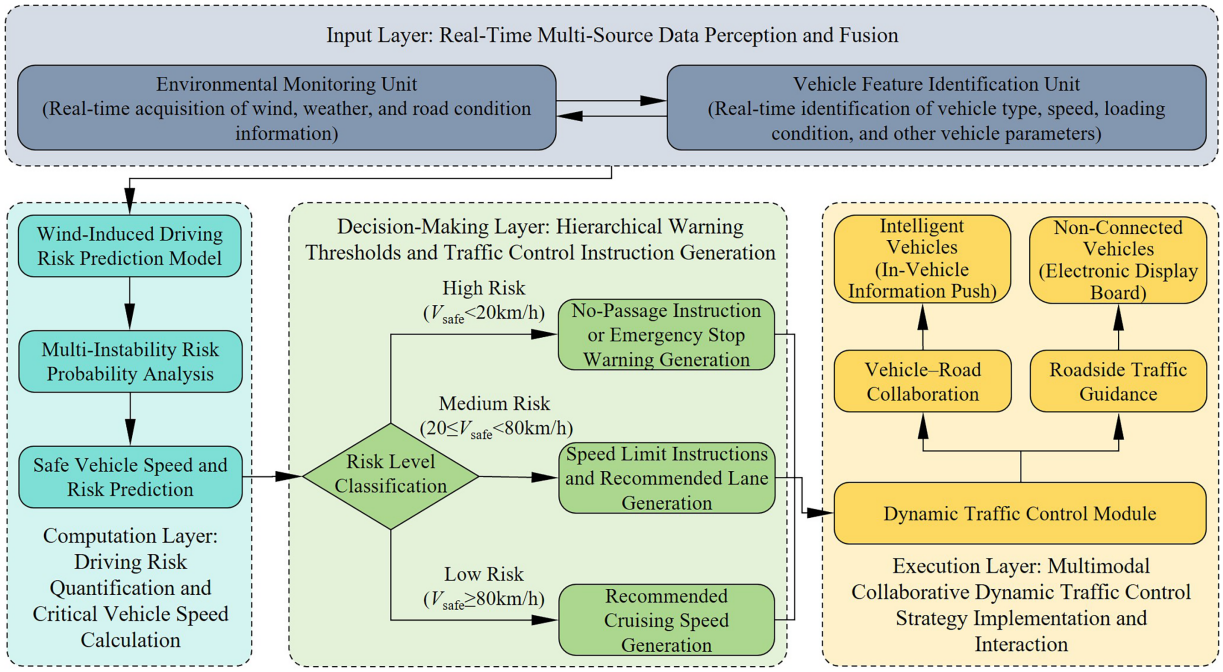


Figure 21: Conceptual traffic management framework for box trucks under crosswind conditions.

Although this control strategy is currently in the stage of theoretical architecture, it bridges the logical chain from underlying physical aerodynamic simulation to top-level machine learning decision-making, aiming to provide a solid algorithmic foundation and prospective engineering theoretical guidance for the research and development of the next-generation smart bridge "holographic perception-intelligent decision-making-collaborative control" integrated system.

(1) Input Module: This module is primarily responsible for the real-time collection and spatiotemporal alignment of multi-source heterogeneous information, consisting of an environmental monitoring unit and a vehicle feature recognition unit. The environmental end monitors flow field data (including

crosswind speed and wind direction angle) at the bridge deck height in real time using ultrasonic anemometers installed on both sides of the bridge. Road adhesion conditions are comprehensively determined via rainfall sensors and pavement condition detectors. Vehicle perception: key parameters such as vehicle type, load, and speed are obtained in real time through the bridge deck dynamic weighing system.

(2) Computation Module: This module applies the trained XGBoost model to the standard box truck considered in this study. By integrating real-time crosswind speed, road-condition information, and the loading condition of the box truck obtained from the weigh-in-motion (WIM) system, the system predicts three types of wind-induced vehicle instability, namely lateral deviation, sideslip, and rollover, and further determines the corresponding recommended safe vehicle speed.

(3) Decision-Making Module: Based on the prediction results, this module compares the current vehicle speed with the predicted safe vehicle speed and generates the corresponding traffic-control instructions. When the current vehicle speed does not exceed the predicted safe speed, the vehicle remains in the normal operating state. When the current speed exceeds the predicted safe speed, a speed-reduction instruction is issued, with the predicted safe speed adopted as the recommended control target. When the predicted safe speed falls below the minimum operating threshold of 20 km/h specified in this study, temporary suspension of vehicle passage is recommended.

(4) Execution Module: The system disseminates the corresponding traffic-control information through variable message signs (VMSs) installed on the bridge deck and, when V2I communication is available, transmits warning messages directly to vehicles. For the box-truck operating conditions investigated in this study, the system issues either a recommended safe vehicle speed or a traffic-suspension warning according to the predicted safety state.

7 Conclusions

(1) Among the multi-dimensional influencing factors of wind-induced driving safety for trucks on bridges, the vehicle payload state plays a decisive role. The vehicle loading condition significantly affects crosswind driving safety by simultaneously altering the total vehicle mass, moments of inertia, vertical tire loads, and center-of-gravity position. Although the center-of-gravity height under the laden condition is higher than that under the unladen condition, the stabilizing effects associated with the greater vehicle mass, inertia, and vertical tire loads are dominant. Furthermore, the laden condition results in reduced aerodynamic rolling and yawing moments acting on the vehicle, thereby further decreasing the risks of rollover and sideslip under crosswind disturbances. Consequently, the laden vehicle exhibits better overall crosswind stability than the unladen vehicle. Road adhesion coefficient, crosswind speed, and vehicle speed are secondary yet critical risk-inducing factors. Crosswind and vehicle speeds exhibit a strong negative correlation with the vehicle's wind-induced driving safety capacity, whereas the road adhesion coefficient shows a strong positive correlation. By contrast, the driver's preview time has the least impact on transient stability indices, such as the peak lateral acceleration.

(2) Vehicle instability in crosswind environments is not merely a sudden change in a single motion, but rather a complex coupling of lateral deviation, sideslip, and yaw, which is also significantly affected by the shielding effect of the bridge. Compared with the unladen condition, the laden vehicle exhibits better crosswind resistance and recovery capability due to its larger overall inertia and greater vertical tire loads. Although the lateral displacement of the vehicle center of gravity is not necessarily smaller under certain operating conditions, the yaw response is significantly reduced. Consequently, when the overall vehicle profile displacement is considered, the laden vehicle demonstrates a lower risk of lateral deviation. When evaluating lateral deviation safety, the superimposed effects of the lateral displacement of the center of mass and the yaw angle must be comprehensively considered. Higher wind and vehicle

speeds exacerbate the lateral deviation and yaw motions of unladen box trucks; encountering a low road adhesion coefficient will further breach the saturation limit of tire cornering force, making the truck highly susceptible to severe sideslip or even rollover accidents. In addition, auxiliary structures such as bridge deck barriers exert a significant blocking and shielding effect on the airflow; their substantial attenuation effect on the actual equivalent effective crosswind speed must be taken into account during evaluation.

(3) Extreme Gradient Boosting (XGBoost) can effectively capture the nonlinear variation in the wind-induced driving risk of box trucks under the coupled effects of multiple influencing factors and demonstrates good predictive performance within the scope of the current simulation dataset. The model outputs show good consistency with the vehicle-dynamics instability criteria and their corresponding trends, indicating that the proposed method can, to a certain extent, reflect the underlying vehicle-dynamics mechanisms. Based on the predicted and fitted safe vehicle speeds, recommended safe speeds under different crosswind speeds and road adhesion conditions can be rapidly determined, thereby providing a computational reference for dynamic speed-limit control. On this basis, a conceptual intelligent bridge traffic management framework for standard box trucks is proposed. By integrating real-time wind-field information, road-surface conditions, and vehicle loading information, the framework generates control recommendations including normal operation, speed-limit intervention, and traffic suspension, while warning information can be disseminated through variable message signs or V2I communication. The practical engineering applicability of this framework still requires further validation using heterogeneous vehicle types, mixed traffic flows, and field-measured data.

(4) Although the XGBoost algorithm demonstrates favorable predictive capabilities, the proposed framework is inherently limited by its reliance on simulation-generated datasets, simplified aerodynamic environments (such as pure 90° crosswinds and fixed turbulence intensities), and idealized vehicle dynamics assumptions (such as rigid bridge decks and deterministic driver models). Therefore, the safety boundaries derived in the present study should be interpreted as deterministic theoretical baselines under the prescribed crosswind conditions, rather than as universally applicable safety envelopes for real atmospheric environments. To achieve practical deployment in smart bridge management, future research must prioritize bridging the "simulation-to-reality" gap. This will require accounting for the impacts of actual bridge types and topography, incorporating real on-site monitored traffic and meteorological data, and utilizing more advanced machine learning paradigms—such as transfer learning or physics-informed continuous calibration—to dynamically generalize the prediction model to complex, real-world operational conditions.

8 Limitations and Future Work

This study proposes an intelligent early warning framework for wind-induced driving safety on cross-sea bridges that integrates high-fidelity physical simulations with cutting-edge machine learning. Although the underlying aerodynamic data have been validated by wind tunnel experiments and the dynamics model incorporates preview control theory, a critical evaluation of the inherent limitations of this methodology is still necessary as it transitions from theoretical deduction to complex engineering practice.

First, the flow-field simulations in this study were conducted using the URANS approach, whose turbulence-averaging and numerical-dissipation characteristics may lead to an underestimation of certain transient peaks in the lateral aerodynamic loads. In addition, a fixed crosswind direction of 90° and a prescribed inlet turbulence intensity were adopted. Therefore, the resulting safety boundaries should be interpreted as deterministic theoretical baselines under the specified uniform crosswind conditions rather

than as universally conservative envelopes for transient wind-induced instability in realistic atmospheric environments. The wind environment over actual cross-sea bridges is characterized by pronounced multi-scale turbulence and stochastic gusts, which may induce transient aerodynamic loads and vehicle-dynamic peak responses exceeding those predicted by the present deterministic simulations. Consequently, the current prediction boundaries are primarily applicable to the prescribed crosswind conditions considered in this study, and their extrapolation to complex stochastic wind environments should be undertaken with caution. Additionally, to accommodate the computational demands of machine learning for massive datasets, the current model simplifies the bridge to a rigid pavement, omitting the structural aeroelastic coupled dynamic interactions of the "Wind-Vehicle-Bridge" (WVB) system. Finally, the framework relies on the rational MacAdam preview control model, which fails to adequately encompass highly stochastic human driving behaviors under extreme crosswinds, such as fatigue, panic-induced over-correction, and cognitive delays. In addition, the validation procedure adopted in the present study mainly relied on random data splitting and conventional 5-fold cross-validation. Stratified partitioning specifically designed for multi-label distributions, nested cross-validation, and explicit grouping of closely related simulation scenarios were not employed. Therefore, the model performance reported in this study primarily reflects internal validation results obtained from the current simulation dataset. Future work will further adopt grouped and nested cross-validation strategies to provide a more rigorous assessment of the model's generalization performance.

Second, the currently derived safe vehicle speed boundaries exhibit strong "scenario specificity." On one hand, the conclusions heavily depend on the specific geometric porosity (75%) of the double-layer barrier, and the strong aerodynamic shielding effect of this barrier results in an extreme imbalance of rollover samples in the dataset. This objectively limits the extrapolation reliability of the model to different bridge windbreak structures. On the other hand, the study exclusively targets standard box trucks driving in isolation, failing to cover heterogeneous vehicles like tractor-semitrailers or account for the aerodynamic interference effects between adjacent vehicles in actual mixed traffic flows.

Lastly, the purely simulated dataset lacks consideration for random perturbations in the real physical world, such as roadside sensor measurement noise, onboard IMU drift, and abrupt changes in friction coefficients caused by localized water pooling. Furthermore, the study has not yet explicitly decoupled the impacts of Vehicle-to-Infrastructure (V2I) communication delays, edge computing processing bottlenecks, and drive-by-wire chassis execution lags through Hardware-in-the-Loop (HiL) testing. Therefore, the current model outputs should be regarded as conceptual speed limit baselines, necessitating the introduction of dynamic safety margins in actual operations.

To address the aforementioned limitations, future research will advance from both data source and engineering practice perspectives. On one hand, high-fidelity methods such as Large Eddy Simulation (LES) will be introduced to finely resolve transient flow fields, expanding the vehicle dynamics database to encompass three-dimensional stochastic fluctuating wind fields, multi-source heterogeneous fleets, and random driver behaviors, while explicitly incorporating dynamic WVB coupling effects. On the other hand, using the deterministic simulation model as a pre-trained baseline, an HiL validation platform integrating real meteorological and onboard sensor data will be established. In practical deployment, transfer learning and online incremental learning strategies will be introduced, utilizing real-vehicle dynamic trajectories and on-site friction estimations captured by the V2I system to dynamically fine-tune the model, thereby comprehensively enhancing the robustness of the intelligent early warning framework in complex, real-world environments.

Acknowledgement: Not applicable.

Funding Statement: This study was supported by the National Natural Science Foundation of China (Nos. 52278537 and 52408558) and the Open Fund of Fujian Provincial Key Laboratory of Wind Disaster and Wind Engineering (No. KF20250204) and Fujian Provincial Natural Science Foundation (2026J0011530) and Major Science and Technology Project of Xiamen Key Innovation Platforms (3502Z20261002).

Author Contributions: Zhiqun Yuan: conceptualization, writing—review and editing, writing—original draft. Maoxing Zhu: writing—original draft, visualization, formal analysis. Shihao Tan: methodology, writing—original draft, software. Hongzheng He: methodology, writing—original draft, software. Yongchen Peng: resources, validation, investigation. Dandan Xia: investigation, methodology. Huaifeng Wang: validation, data curation. Li Lin: conceptualization, resources, supervision, project administration, funding acquisition. All authors reviewed and approved the final version of the manuscript.

Availability of Data and Materials: The data that support the findings of this study are available from the corresponding author upon reasonable request.

Ethics Approval: Not applicable.

Conflicts of Interest: The authors declare no conflicts of interest.

References

1. Sivaramakrishnan P, Madhava Prakash AK, Sekulic D, Jacobson B, Selvi C, Johannesen SM. Methods to introduce floating bridge motion and wind excitation on a model for the investigation of heavy vehicle dynamics. Appl Math Model. 2023;117(5):118–41. doi:10.1016/j.apm.2022.11.038.
2. Zhou Y, Xue F, Zhang B, Tian H, Xie F, Sun P, et al. Model predictive control for multi-axis steering trajectory tracking strategy of heavy-duty articulated vehicle with vehicle status accurate estimation. Results Eng. 2025;27(9):106580. doi:10.1016/j.rineng.2025.106580.
3. Alika R, Mellouli EM, Tissir EH. A modified sliding mode controller based on fuzzy logic to control the longitudinal dynamics of the autonomous vehicle. Results Eng. 2024;22(4):102120. doi:10.1016/j.rineng.2024.102120.
4. Goli M, Ghodrati B, Eleftheroglou N. A literature review-based evaluation framework for maintenance strategy selection in heavy vehicles. Results Eng. 2025;28(2):107109. doi:10.1016/j.rineng.2025.107109.
5. He J, Xiang H, Li Y, Han B. Aerodynamic performance of traveling road vehicles on a single-level rail-cum-road bridge under crosswind and aerodynamic impact of traveling trains. Eng Appl Comput Fluid Mech. 2022;16(1):335–58. doi:10.1080/19942060.2021.2012516.
6. Huang T, Feng M, Huang J, Ma J, Yi D, Ren X, et al. Aerodynamic stability of vehicle passing through a bridge tower at high speed under crosswind conditions with different road adhesion coefficients. Alex Eng J. 2023;77(3):461–78. doi:10.1016/j.aej.2023.07.001.
7. Du X, Wang G. Analysis of operating safety of tractor-trailer under crosswind in cold mountainous areas. Appl Sci. 2022;12(24):12755. doi:10.3390/app122412755.
8. Yao Z, Zhang N, Zhu M, Li X. Dynamic interaction analysis and running safety assessment of the wind–train–bridge system considering the moving train's aerodynamic coupling with crosswind. Int J Struct Stab Dyn. 2023;23(15):2350173. doi:10.1142/s0219455423501730.
9. Ali Y, Hussain F, Haque MM. Advances, challenges, and future research needs in machine learning-based crash prediction models: a systematic review. Accid Anal Prev. 2024;194:107378. doi:10.1016/j.aap.2023.107378.
10. Said Y, Alassaf Y, Ghodbani R, Saidani T, Ben Rhaiem O. Deep learning-driven pattern recognition for real-time traffic incident detection in complex urban environments. Trait Signal. 2025;42(2):975–83. doi:10.18280/ts.420231.
11. Yang Y, Wang K, Yuan Z, Liu D. Predicting freeway traffic crash severity using XGBoost-Bayesian network model with consideration of features interaction. J Adv Transp. 2022;2022(1):4257865. doi:10.1155/2022/4257865.

12. Tang J, Huang Y, Liu D, Xiong L, Bu R. Research on traffic accident severity level prediction model based on improved machine learning. Systems. 2025;13(1):31. doi:10.3390/systems13010031.
13. Parsa AB, Movahedi A, Taghipour H, Derrible S, Mohammadian AK. Toward safer highways, application of XGBoost and SHAP for real-time accident detection and feature analysis. Accid Anal Prev. 2020;136:105405. doi:10.1016/j.aap.2019.105405.
14. Li H, Chen L. Traffic accident risk prediction based on deep learning and spatiotemporal features of vehicle trajectories. PLoS One. 2025;20(5):e0320656. doi:10.1371/journal.pone.0320656.
15. Sharma P, Chung WT, Akoush B, Ihme M. A review of physics-informed machine learning in fluid mechanics. Energies. 2023;16(5):2343. doi:10.3390/en16052343.
16. Mochalin I, Wang J, Cai J, E. S. Enhancement of physics-informed neural networks in applications to fluid dynamics. Phys Fluids. 2025;37(5):057130. doi:10.1063/5.0269943.
17. Cheng L, Lei D, Tao S. Recent advances in deep learning for traffic probabilistic prediction. Transp Rev. 2024;44(6):1129–35. doi:10.1080/01441647.2024.2408840.
18. Manikandan BV, Nathan TR, Naresh R, Prasad P. Traffic flow prediction for intelligent transportation system using machine learning. E3S Web Conf. 2023;387(4):05002. doi:10.1051/e3sconf/202338705002.
19. Ying L, Jin L, Guan Y. Collaborative physics-informed neural dynamics approach for autonomous vehicles with nonconvex safety-critical constraints. IEEE Trans Intell Transp Syst. 2025;26(10):16887–98. doi:10.1109/TITS.2025.3572336.
20. Seyyedi A, Bohlouli M, Oskoee SN. Machine learning and physics: a survey of integrated models. ACM Comput Surv. 2024;56(5):115. doi:10.1145/3611383.
21. Xu S, Dai Y, Yan C, Sun Z, Huang R, Guo D, et al. On the preprocessing of physics-informed neural networks: how to better utilize data in fluid mechanics. J Comput Phys. 2025;528(6):113837. doi:10.1016/j.jcp.2025.113837.
22. Zhang J, Chen H, He Y. Physics-informed adaptive deep Koopman operator modeling for autonomous vehicle dynamics. Adv Eng Inform. 2026;71(2):104274. doi:10.1016/j.aei.2025.104274.
23. Li Y, Liu L. Physics-informed neural network-based nonlinear model predictive control for automated guided vehicle trajectory tracking. World Electr Veh J. 2024;15(10):460. doi:10.3390/wevj15100460.
24. Yuan Z, Lu H, Lin L, Lin X, Gao X. Study on crosswind stability of van truck on sea-crossing bridge. Automot Eng. 2021;43(8):1238–47. doi:10.19562/j.chinasae.qcgc.2021.08.016.
25. Chen Y, Djidjeli K, Xie ZT. Freestream turbulence effects on the aerodynamics of an oscillating square cylinder at the resonant frequency. Fluids. 2022;7(10):329. doi:10.3390/fluids7100329.
26. Kaluva ST, Pathak A, Ongel A. Aerodynamic drag analysis of autonomous electric vehicle platoons. Energies. 2020;13(15):4028. doi:10.3390/en13154028.
27. Ashton N, West A, Lardeau S, Revell A. Assessment of RANS and DES methods for realistic automotive models. Comput Fluids. 2016;128(1):1–15. doi:10.1016/j.compfluid.2016.01.008.
28. Zhang Z, Li J, Guo W. Combined simulation of heavy truck stability under sudden and discontinuous direction change of crosswind with computational fluid dynamics and multi-body system vehicle dynamics software. Adv Mech Eng. 2018;10(7):1687814018786364. doi:10.1177/1687814018786364.
29. Brandt A, Jacobson B, Sebben S. High speed driving stability of road vehicles under crosswinds: an aerodynamic and vehicle dynamic parametric sensitivity analysis. Veh Syst Dyn. 2022;60(7):2334–57. doi:10.1080/00423114.2021.1903516.
30. Carbonne L, Winkler N, Efraimsson G. Use of full coupling of aerodynamics and vehicle dynamics for numerical simulation of the crosswind stability of ground vehicles. SAE Int J Commer Veh. 2016;9(2):359–70. doi:10.4271/2016-01-8148.
31. MacAdam CC. Application of an optimal preview control for simulation of closed-loop automobile driving. IEEE Trans Syst Man Cybern. 1981;11(6):393–9. doi:10.1109/TSMC.1981.4308705.
32. Yuan Z, Huo D, Chen Y, Xia D, Wang H, Lin L. Vehicle lateral control and stability analysis under the disturbed flow coupling effect in the crosswind region of a bridge tower. Int J Dyn Control. 2025;13(11):388. doi:10.1007/s40435-025-01888-z.

33. Yan M, Xu J, Han S, Xin T, Wang O, Yi Z, et al. Permitted speed decision of single-unit trucks with emergency braking maneuver on horizontal curves under rainy weather. PLoS One. 2021;16(12):e0261975. doi:10.1371/journal.pone.0261975.
34. Kobayashi T, Katsuyama E, Sugiura H, Ono E, Yamamoto M. Efficient direct yaw moment control: tyre slip power loss minimisation for four-independent wheel drive vehicle. Veh Syst Dyn. 2018;56(5):719–33. doi:10.1080/00423114.2017.1330483.
35. Shi X, Wong YD, Li MZ, Palanisamy C, Chai C. A feature learning approach based on XGBoost for driving assessment and risk prediction. Accid Anal Prev. 2019;129(1):170–9. doi:10.1016/j.aap.2019.05.005.
36. Ustun B, Spangher A, Liu Y. Actionable recourse in linear classification. In: Proceedings of the Conference on Fairness, Accountability, and Transparency. New York, NY, USA: The Association for Computing Machinery (ACM); 2019. p. 10–9. doi:10.1145/3287560.3287566.
37. Nocedal J, Wright SJ. Numerical optimization. 2nd ed. New York, NY, USA: Springer; 2006. doi:10.1007/978-0-387-40065-5.
38. Cheli F, Corradi R, Sabbioni E, Tomasini G. Wind tunnel tests on heavy road vehicles: cross wind induced loads: Part 1. J Wind Eng Ind Aerodyn. 2011;99(10):1000–10. doi:10.1016/j.jweia.2011.07.009.